eHeroes D3.5
Source regions, acceleration mechanisms and interplanetary propagation of Solar Energetic Particles

Project acronym: *EHEROES*
Project title: *Environment for Human Exploration and RObotic Experimentation in Space*
Grant Agreement number: *284461*
Coordinator: *Giovanni Lapenta*
Project co-funded by the European Commission,
Seventh Framework Programme
Funding Scheme: *FP7-SPACE-2011-1*

Due date of deliverable:	**Month 30**
Actual submission date:	**Month 32**
Start date of the project:	**March 1, 2012**
Project duration:	**3 years**

Work package:	**3**
Task(s):	**3.6**
Lead beneficiary for this deliverable:	**UGOE**
Editor:	**V. Bothmer**
Authors:	**V. Bothmer, R. Kanzler, A. Pluta**
Quality reviewer:	**V. Bothmer, L. van Driel-Gesztelyi**

NOTICE

Table of Contents

1. Introduction

Solar energetic particles can cause damage or failure of spacecraft electronic systems and pose higher-than-normal radiation doses for crew members of spacecraft and high-flying aircraft, which can affect physical health (e.g., ref.).

The University of Göttingen led eHEROES Task 3.6 "Source region, acceleration mechanisms and interplanetary propagation of SEPs", as part of eHEROES Work Package 3 "Solar and Space Events and their Evolution". The achievements of this task are summarised through the eHEROES deliverable D3.5 „Source region, acceleration mechanisms and interplanetary propagation of SEPs". Contributing partners to D3.5 were UCL, UCT, LPI.

The main goal of D3.5 can be summarised as follows: "eHEROES deliverable D3.5 aims at deriving quantitative results about the intensity dependence of major solar energetic particle events in the inner heliosphere on the magnetic coupling to the solar source regions and the extrapolation of these results to the orbit of Mars for future space applications".

The following sections of this report summarise the results of the eHEROES activities for this deliverable after a brief summary of background knowledge needed to better understand the causes and mechanisms of solar energetic particle events (SEP events).

2. Summary of basic knowledge

2.1 Solar wind and interplanetary magnetic field as background medium

Solar energetic particles propagate within the heliosphere in the solar wind and its embedded interplanetary magnetic field. The following section provides a brief summary about the basic properties of the solar wind as background medium. For a more detailed summary the reader is referred to chapter 3 „The Sun as prime source of space weather" of Bothmer and Daglis (2007).

A steady stream of plasma flows from the Sun outward into the solar system and forms the heliosphere. This solar wind consists mostly of electrons and protons with energies between 1.5 keV and 10 keV and carries the solar magnetic field, which then becomes the interplanetary magnetic field (IMF).

The source regions of the solar wind rotate with the Sun and create a spiral magnetic field structure, which was first predicted by Parker (1958) and was named after him. Figure 1 shows a two-dimensional schematic of the Parker spiral for two different solar wind speeds of 400 km/s and additionally for a 2.000 km/s high speed case eventually reached in shock associated coronal mass ejection flows. The orbits of Earth and Mars are also shown. Depending on the solar wind speed v_R at a given distance R and the rotational velocity of the Sun the direction angle φ of the magnetic field is

$$\varphi = \left| \frac{\omega_\odot R}{v_R} \right|$$

The polarity of the solar wind magnetic field depends on the polarity of the solar wind source region magnetic field: if the magnetic field is directed towards the Sun it has so called negative polarity, whilst it has positive polarity if it is outward directed. Through the solar wind „Parker spiral" structure an observer is magnetically connected to the solar wind source region at times of a SEP event. This information is provided by continuous measurements of the ACE (Advanced Composition Explorer) satellite orbiting in an L1 orbit and during some periods in time also by the WIND satellite. Typically the solar wind occurs in form of slow and fast solar wind streams with velocities of 300 to 800 km/s.
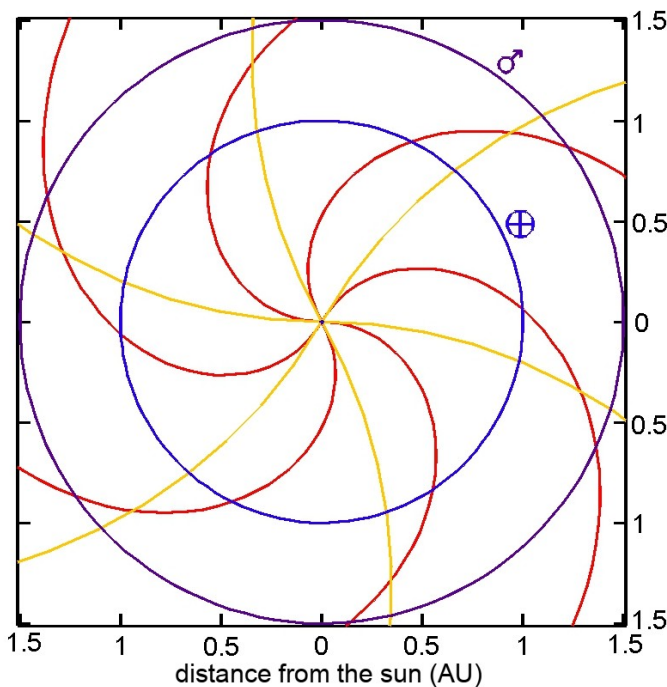
Figure 1. Schematic view of the Parker spiral structure in the solar equatorial plane for solar wind speeds of 400 km/s (red) and 2000 km/s (yellow). The orbit blue circle is the orbit of Earth, the violet one is the orbit of Mars. Credit: NASA.

2.2 Fast coronal mass ejections (CMEs) and solar energetic particles (SEPs)

Transient solar wind flows, often associated with interplanetary shocks, can reach velocities of 2000 km/s and above (e.g., Bothmer (1999)). They are driven by coronal mass ejection (CME) at the Sun. CMEs expand outward into the heliosphere with speeds from several hundreds up to 3000 km/s or above close to the Sun. Figure 2 shows a CME that was observed on February 27, 2000 by the coronagraphs on board the SOHO spacecraft. When observed in interplanetary space, a CME is commonly called interplanetary CME (ICME). Measuring the movement of the ICME's leading edge over time makes it possible to determine the speed of the ICME. In very fast CME events, shocks may be directly observed in white-light coronagraph images (Vourlidas et al., 2003).
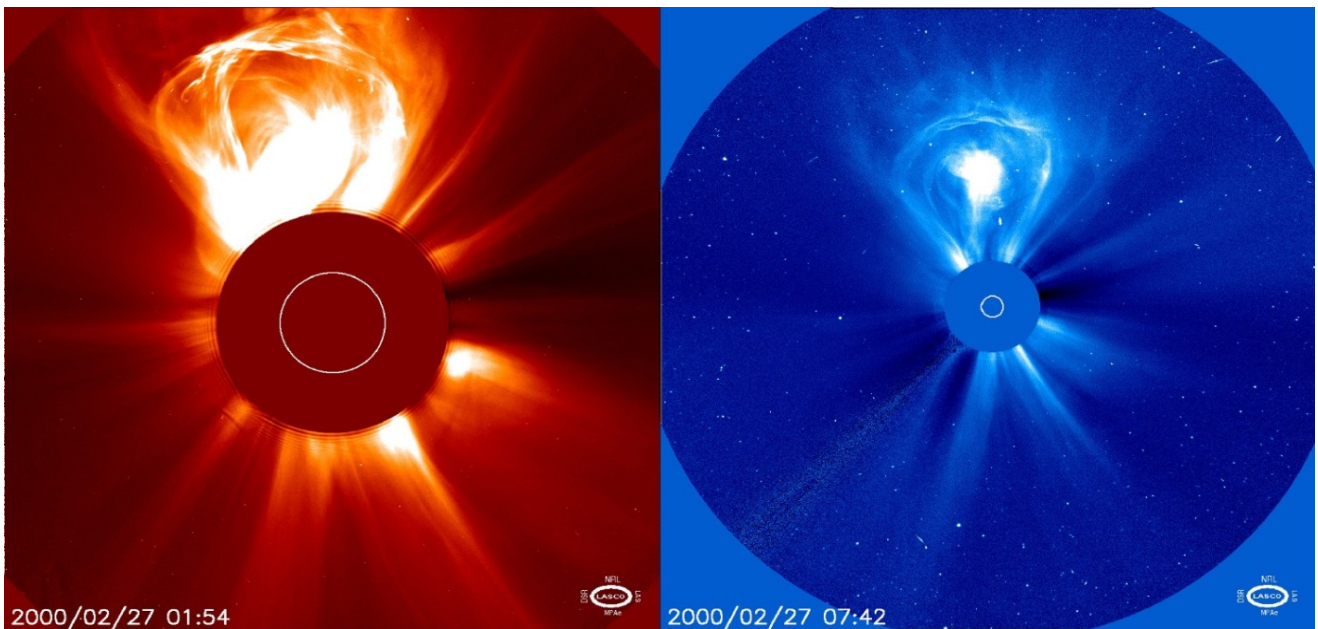
Figure 2. Coronal mass ejection observed on February 27, 2000 by the SOHO/LASCO C2 (left) and C3 (right) coronagraphs. The CME can be seen because the bright solar disk is covered by occulter. Credit: SOHO.

Fast CMEs with velocities greater than about 750 km/s drive interplanetary shocks and charged particles can be accelerated through the physical mechanism of diffusive shock acceleration (e.g., Reames et al., 1997), also known as first order Fermi acceleration (Fermi, 1949). At the shock, the magnetic field of the moving plasma is inhomogeneous so that protons, travelling across the shock can be reflected through propagating changes in the magnetic field and gain energy, e.g. in the case of self-generated Alfvén waves (e.g., Swanson 1989, Reames, 2001). The question of particle injection into the acceleration region however is still unresolved. One theory assumes acceleration of protons from the ambient solar wind, another one assumes independently created energetic seed protons injected from a suprathermal pool. Neergaard, Parker and Zank (2012) showed that contrary an injection energy of 1.05 keV to 2.785 keV would ensure that the intensity of the theoretical

accelerated ion spectrum matches the observed spectrum and that protons could be accelerated directly out of the solar wind, without the need for suprathermal seed protons.

Another process of particle acceleration assumes changes in the configuration, called magnetic reconnection, of strong local magnetic fields in solar active regions. In this way energy that was conserved by the magnetic field can be transformed into kinetic and thermal energy in form of electromagnetic radiation as solar flares, also accelerating charged particles. The acceleration process is of short duration compared to the acceleration of particles at interplanetary shocks (e.g., Cane et al., 2006).

2.3   Solar energetic proton events

Solar energetic protons can be generated by diffusive shock acceleration at the shock of CMEs or through magnetic reconnection near the solar surface in solar flares, as explained above. Differences in composition and time profiles of corresponding particle events lead to the classification into impulsive (thought to be accelerated through magnetic reconnection in flares) and gradual (thought to be accelerated by the shocks of CMEs) particle events. A visualization of the different acceleration regions is shown in Figure 3. While impulsive events last only a few hours (e.g. Cliver & Cane, 2002), gradual events can last several days and have higher intensities (e.g. Reames, 1999). The strongest SEP events are due to gradual events (Reames, 2004).
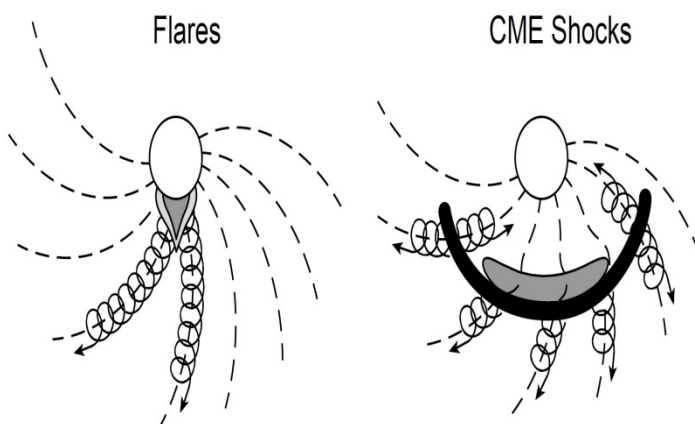
Figure 3. Comparison of the acceleration regions of impulsive particle events (left) and gradual particle events (right). Because of the spatial extent of the shock (black bar), the acceleration of particles occurs in a larger region than particle acceleration in solar flares (Reames, 1999).

Simulation from Ng & Reames (2008) showed that for shock velocities of 2500 km/s, protons get accelerated to energies of up to 300 MeV during the first ten minutes of the acceleration process. As a sample event, Figure 4 shows the SEP event of January 17, 2005.
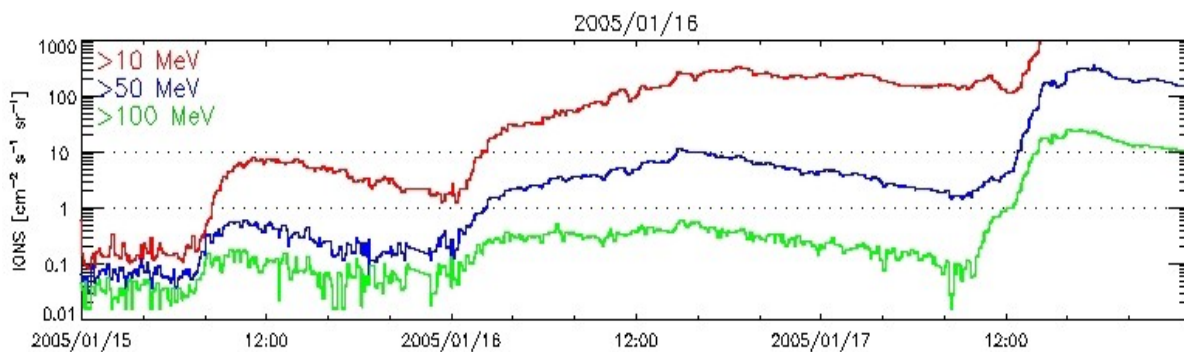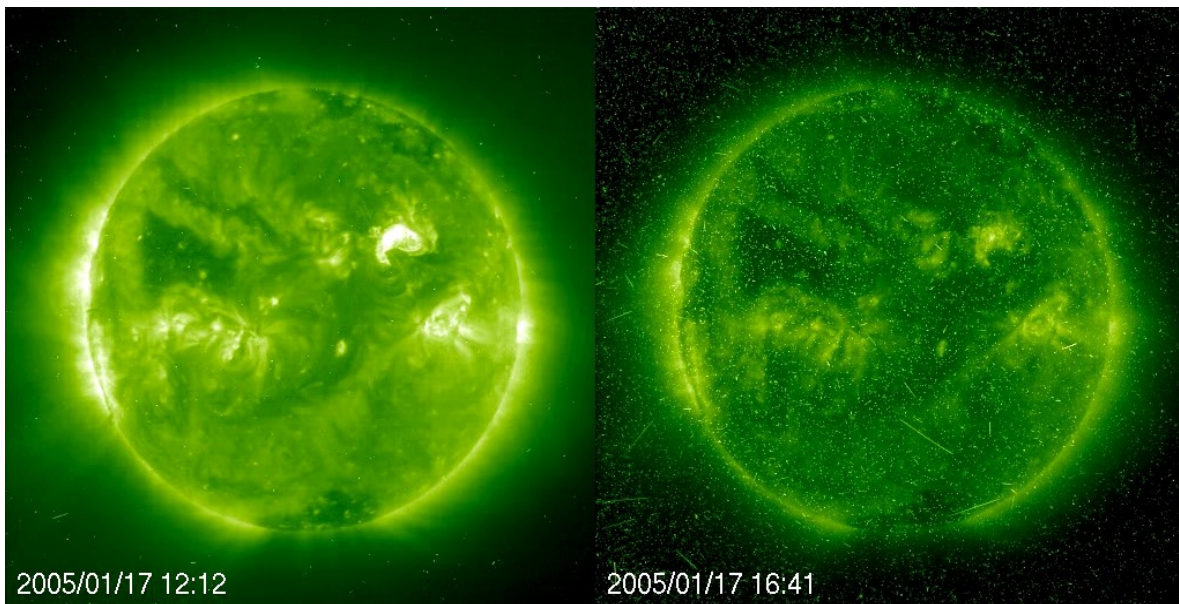
Figure 4. Solar proton event on January 17, 2005. Above: SOHO EIT 19.5 nm image just before (left) and near the maximum of the event (right). The „snowstorm" on the right image is caused by the particles which hit the EIT CCD. Below: Time profile of the proton flux from GOES satellite measurements. The maximum proton flux for E>10 MeV is off the scale at 5040. Credit: SOHO/EIT and SOHO LASCO CME Catalog.

Comparing the intensity time profiles of gradual solar energetic proton events for different heliographic longitudes, these profiles differ as shown in Figure 5 (Cane and Lario, 2006). The different intensity time profiles reflect the influence of the Parker spiral on particle propagation and indicate that the magnetic connection of an observer to the shock associated CME and ICME and solar source region should play an important role in determining the observed strength and time profile of an individual event.
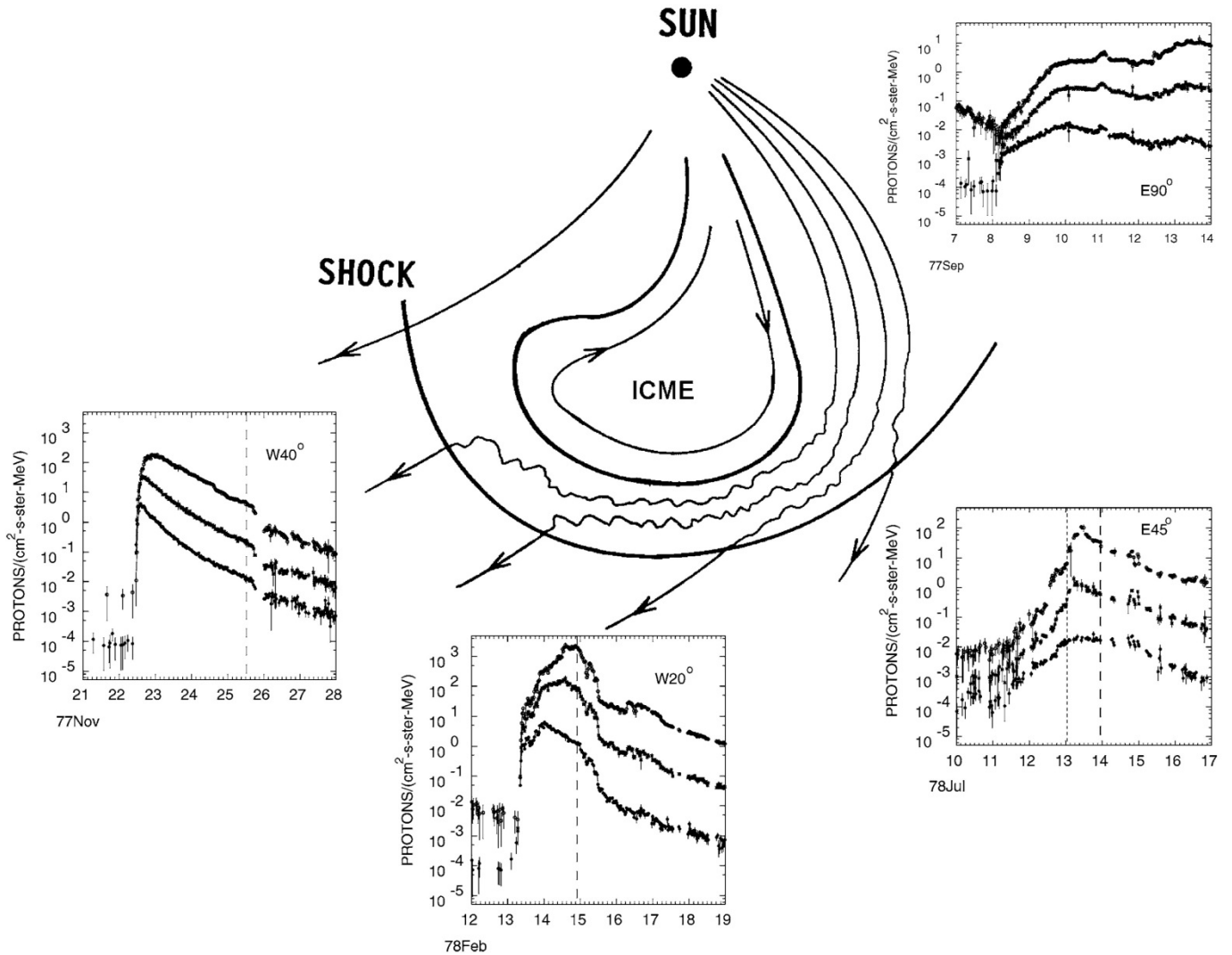
Figure 5. Intensity-time profiles of solar proton events for the observation at different heliographic longitudes with respect to the CME/ICME driven shock (Cane & Lario, 2006).

2.4 Measurement of solar energetic protons

Particle detectors count the number of incident particles within a field of view and in a predefined energy range or above. A particle which hits the detector loses kinetic energy to the detector surface, where atoms or molecules get ionized or excited and charge carriers get released, counted and the result are digitized. Detectors are differently designed for particular types of particles, provides measurements of particle counts, energies and velocities.

2.5   Particle radiation

Solar energetic protons are ionizing particle radiation because their kinetic energy is sufficient to separate one or more electrons from an atom or molecule. Thereby an energetic proton ionizes atoms directly through Coulomb forces. The ionization of atoms or molecules within the human body and in technology like satellite electronics can cause temporary and permanent damage, depending on the energies and the intensity of the radiation and the duration of the exposure.

Ionizing radiation in general is measured through the absorbed energy per mass (usually in units of Gray, 1 Gy=1 J/kg). For consideration concerning biological effects, this dose is altered with the relative biological effectiveness (RBE), a factor that depends on the type of radiation. For protons this factor is 2 (Valentin, 2003) and so the equivalent dose for protons, measured in Sievert (J/kg) is twice the absorbed energy per mass. Higher concentrations of ionization confer larger molecular and hence biological damage. Radiation doses of 50 mSv per year (in the United States of America) and doses below 200 mSv are considered chronic low dose exposure, while doses above 3 Sv are ultra-high exposures, where early mortality is likely (to be found e.g., in Bothmer & Daglis, 2007). In Europe the radiation dose limit for work-related exposure is 20 mSv per year and 400 mSv for the whole professional life. For comparison, a single full-body CT scan generates a radiation dose of 10 to 30 mSv, while the global average of natural background radiation is 2.4 mSv per year.

Radiation effects on humans are categorized into early effects that occur some hours to several weeks after exposure and late effects, which appear years or decades after exposure. Extreme doses can even have effects after some minutes. Acute effects occur when the rate of cell killing is higher than the rate of cell recovery and the remaining cells cannot maintain the tissue function. The principal late effect is carcinogenesis and late mortality from cancer is the reference risk to derive exposure limits. The Earth's atmosphere is a protective layer that shields the planet's surface from most solar energetic protons, and the Earth's magnetosphere provides some protection for spacecraft in low-altitude orbit. Nevertheless, crews of high-flying aircraft experience increased radiation doses and astronauts are completely outside of the atmosphere, which increases the chance of radiation hazards. To reduce the risk of radiation exposure for astronauts, spacesuits for extravehicular activity are hardened to shield low energy radiation. For example, a spacesuit with 1 mm thickness can shield radiation with energies up to 1 MeV. Using aluminium as shield material, this limit is extended to 40 MeV.

The walls of spacecraft also shield radiation with low energies, but high energetic particles generate harmful secondary radiation when they strike metals (Hanslmeier, 2002), increasing the overall radiation dose. Energetic solar protons also affect electronics of high-flying aircraft, satellites in Earth orbit, and other spacecraft inside or outside the Earth's magnetosphere. The impact of protons can cause component and material degradation, as well as the temporary or permanent disruption of system operation. The basic permanent damage mechanisms in semiconductor devices exposed to high-energy protons are accumulated ionization effects and atomic displacements in semiconductors. In general, however, effects of proton exposure on the internal electronics are dominated by the ionizing energy deposition (Stassinopoulos & Raymond, 1988). But also single-event effects occur, where a high energetic charged particle travels through a semiconductor ionizing the surrounding material and causing e.g. state changes of memory bits. To prevent those effects, electronics is hardened, e.g. through insulation and shielding. Increased redundancy of critical electronic hardware can improve the reliability of instruments to compensate disturbances of measurements or communications.

2.6   NOAA space weather radiation scale

The space weather scales, created and provided by the US National Oceanic and Atmospheric Administration (NOAA) provide an overview on several impacts on humans and technology caused by space weather effects. Figure 6 shows a table describing the NOAA space weather scales for solar radiation storms, i.e. for the effects of SEP radiation. There are also scales for geomagnetic storms and radio blackouts. The effects of solar radiation storms depend on the level of the proton flux (from 10 pfu to 10^5 pfu) at energies >10 MeV. Storms are classified accordingly: minor radiation storms with <100 pfu pose no threat, strong (~ 10^3 pfu), severe (~ 10^4 pfu) and extreme (~ 10^5 pfu) radiation storms have clearly hazardous effects.

Solar Radiation Storms			Flux level of $\geq$ 10 MeV particles (ions)*
Extreme	Biological: unavoidable high radiation hazard to astronauts on EVA (extra-vehicular activity); passengers and crew in high-flying aircraft at high latitudes may be exposed to radiation risk. *** Satellite operations: satellites may be rendered useless, memory impacts can cause loss of control, may cause serious noise in image data, star-trackers may be unable to locate sources; permanent damage to solar panels possible. Other systems: complete blackout of HF (high frequency) communications possible through the polar regions, and position errors make navigation operations extremely difficult.		10^5
Severe	Biological: unavoidable radiation hazard to astronauts on EVA; passengers and crew in high-flying aircraft at high latitudes may be exposed to radiation risk.*** Satellite operations: may experience memory device problems and noise on imaging systems; star-tracker problems may cause orientation problems, and solar panel efficiency can be degraded. Other systems: blackout of HF radio communications through the polar regions and increased navigation errors over several days are likely.		10^4
Strong	Biological: radiation hazard avoidance recommended for astronauts on EVA; passengers and crew in high-flying aircraft at high latitudes may be exposed to radiation risk.*** Satellite operations: single-event upsets, noise in imaging systems, and slight reduction of efficiency in solar panel are likely. Other systems: degraded HF radio propagation through the polar regions and navigation position errors likely.		10^3
Moderate	Biological: passengers and crew in high-flying aircraft at high latitudes may be exposed to elevated radiation risk.*** Satellite operations: infrequent single-event upsets possible. Other systems: effects on HF propagation through the polar regions, and navigation at polar cap locations possibly affected.		10^2
Minor	Biological: none. Satellite operations: none. Other systems: minor impacts on HF radio in the polar regions.		10

* Flux levels are 5 minute averages. Flux in particles·s^{-1}·ster^{-1}·cm^{-2} Based on this measure, but other physical measures are also considered.
** These events can last more than one day.
*** High energy particle (>100 MeV) are a better indicator of radiation risk to passenger and crews. Pregnant women are particularly susceptible.

Figure 6. NOAA space weather scales for solar radiation storms. Radiation storms have different hazardous effects depending on the proton flux level. Adapted from http://www.swpc.noaa.gov/NOAAscales/.

3. Missions, Instruments and Data

The data that were used for the analysis of the solar energetic proton events come from satellites which observe the Sun and from ones which measure the space environmental conditions. In the following sections, the satellites and relevant instruments and data are described.

3.1 ACE – Advanced Composition Explorer

On August 25, 1997 the Advanced Composition Explorer (ACE) satellite, also known as Explorer 71, was launched by the National Aeronautics and Space Administration (NASA) and sent to the Lagrangian point $L1$. ACE consists of nine instruments that provide high-precision measurements on elemental, isotopic, and ionic charge state composition of energetic nuclei over a broad energy range, with time resolution adequate to investigate the dynamical processes affecting the composition (Stone et al., 1998).

The data on the solar wind conditions and its magnetic field parameters, relevant for this study come from the magnetometer (MAG) and the Solar Wind Electron Proton Alpha Monitor (SWEPAM) instruments. SWEPAM measures the three-dimensional characteristics of solar wind and suprathermal electrons from ≈ 1 eV to 900 eV and ions from 0.26 keV to 35 keV. MAG is a flight spare of the WIND satellite's magnetometer and measures the dynamic behaviour of the magnetic field vectors and the magnitude of the magnetic flux density. The ACE spacecraft can also measure solar energetic particles. The EPAM instrument is an Electron, Proton, and Alpha Monitor and detects electrons and ions with energies up to 5 MeV, which is not high enough for the analysis of hazardous SEP events. A more detailed overview of the ACE mission, the satellite and its instruments can be found in Stone et al. (1998).

3.2   GOES – Geostationary Operational Environmental Satellite

The GOES satellite system is operated by the National Environmental Satellite, Data, and Information Service (NESDIS), which is part of NOAA. Since 1975, when the first GOES satellite was launched, the GOES system has used geosynchronous satellites to support weather forecasting and meteorological and atmospheric research, as well as monitoring the satellites environment in space. Today, the system consists of four operational satellites. Aside from instruments for terrestrial observations, the Solar Environment Monitor (SEM) is used for space weather related in-situ measurements within the Earth magnetosphere and consists of several sub- systems. SEM has two magnetometers for magnetic field measurements, an X-ray and EUV sensor (XRS_EUV) that measures the solar X-ray and ultraviolet radiation, an Energetic Particle Sensor (EPS) and a High Energy Proton and Alpha Detector (HEPAD). EPS contains semi-conductor detectors for electrons, protons and alpha particles.

3.3   SOHO – Solar Heliospheric Observatory

As an international joint project between the European Space Agency (ESA) and NASA, SOHO was launched on December 2, 1995 to continue ESA's Solar Terrestrial Science Programme (STSP). The spacecraft was sent to the Lagrangian point $L1$ and began its normal operations in May 1996. During gyroscope calibrations on June 24, 1998, SOHO lost its pointing to the Sun and went into an emergency mode (Emergency Sun Reacquisition, ESR), while the angle between its solar panels and the Sun was almost 90°.

The contact to the satellite was lost on June 25 and it took until August 3 to receive SOHO's carrier signal and restore the communication. On September 16, the pointing towards the Sun was restored and on October 24, 1998 the instrument recovery was finished. At this time only one functional gyroscope was left. On December 21, 1998 this last gyroscope failed and caused the spacecraft to enter the ESR mode again. Normal operation was restored on January 31, 1999 (Roberts, 2002).

The spacecraft has twelve instruments to observe the Sun and heliosphere. The Extreme ultraviolet Imaging Telescope (EIT), the Large Angle and Spectrometric Coronagraph (LASCO) and the Michelson Doppler Imager (MDI) provide data that are important for this study. The EIT observes the solar disk at the EUV wavelengths of 17.1 nm, 19.5 nm, 28.4 nm and 30.4 nm to investigate the solar corona. The original cadence was five images per hour, but it was reduced to two images per hour in August 1, 2010 due to the higher angular and time resolution of SDO. Detailed information on the EIT instrument is provided by Moses et al. (1997). LASCO consists of three coronagraphs (C1, C2 and C3) with overlapping fields of view from 1.1 to 30 R_S (Brueckner et al., 1995). While C1 (1.1 to 3 R_S) uses a Fabry-Pérot interferometer, C2 (1.5 to 6 R_S) and C3 (3.7 to 30 R_S) use white light for imaging. A coronagraph observes the solar corona while the bright solar disk is occulted. This observation method enables the direct study of coronal features like CMEs and the combined field of view of the LASCO coronagraphs makes it possible to investigate the expansion and evolution of CMEs while they move away from the Sun (e.g., Plunkett et al. 1998). MDI measures the velocity and magnetic fields of the photosphere for studies related to helioseimology and the solar magnetic variability. Details on the Solar Oscillations Investigation (SOI) with MDI are described by Scherrer et al. (1995).

3.4 STEREO – Solar Terrestrial Relations Observatory

NASA's Solar TErrestrial RElations Observatory (STEREO) mission was launched on October 26, 2006 and consists of two nearly identical spacecraft which orbit the Sun at about 1 AU. STEREO A (ahead) has an orbit slightly closer to the Sun and therefore moves faster than Earth, increasing its angular distance at 22° per year. The orbit of STEREO B (behind) is slightly further away, resulting in slower orbital velocity than Earth and a loss of 22° per year with respect to Earth. On February 6, 2011 the position of the satellites reached a separation angle of 180°, allowing the observation of the entire Sun for the first time ever. The mission was designed to provide a stereoscopic view of the Sun to study the properties of CMEs and their evolution in the heliosphere, as well as the structure of the solar wind and the acceleration of particles in the lower corona and the interplanetary space.

Both spacecraft are equipped with the same four instruments. The In-situ Measurements of PArticles and CME Transients (IMPACT) instrument measures the three-dimensional distribution of electrons in the solar wind and the properties of the IMF. The PLAsma and SupraThermal Ion Composition (PLASTIC) instrument measures the plasma characteristics of protons, alpha particles and heavy ions. STEREO/WAVES (SWAVES) is an experiment to track radio disturbances on their way from the Sun to Earth. The Sun Earth Connection Coronal and Heliospheric Investigation (SECCHI) is a package that has five cameras which observe the solar corona from the solar disk to over 1 AU. The solar disk and the corona are imaged by the extreme ultraviolet imager (EUVI) and the two white-light corona-graphs (COR1 and COR2), while the heliospheric imagers (HI1 and HI2) observe the space between Sun and Earth (Howard et al., 2008).

3.5   SDO – Solar Dynamic Observatory

The Solar Dynamics Observatory (SDO) is a NASA mission that was launched on February 11 in 2010 to continue and extend the observations of the SOlar and Heliospheric Observatory (SOHO) on a higher level of detail. The satellite is in a geosynchronous orbit and has three instruments that point at the Sun. The Extreme Ultraviolet Variability Experiment (EVE) measures the solar extreme ultraviolet (EUV) irradiance at 0.1 nm to 105 nm with high spectral resolution and temporal cadence to investigate changes on timescales that affect the climate of the Earth. The Atmospheric Imaging Assembly (AIA) observes the complete solar disk at nine different wavelengths of the ultraviolet (UV) spectrum (160 nm and 170 nm) and the EUV spectrum (9.4 nm, 13.1 nm, 17.1 nm, 19.3 nm, 21.1 nm, 30.4 nm and 33.5 nm), as well as in one wavelength of the visible spectrum at 450 nm. The resolution of 1 arcsec and the cadence of 10 seconds provides detailed information on the solar corona and its variability. A detailed description of the instrument can be found in Lemen et al. (2012). Variations of the photospheric magnetic field and velocity field are measured by the Helioseismic and Magnetic Imager (HMI) to decypher the physics of the solar magnetic dynamo. Details on the products of HMI are described by Scherrer et al. (2012). An overview on the mission and the science goals is given by Pesnell et al. (2012).

3.6   WIND

Launched on November 1 in 1994, the WIND satellite measures the solar-terrestrial plasma environment for predictions of Earth atmospheric response due to changes of the solar wind. The spacecraft was planned to go to the Lagrangian point $L1$, but was delayed until 2004 due to the ACE and SOHO spacecraft which had the same destination. WIND has a wide range of instruments to measure the solar wind parameters, energetic particles and high-energy photons like gamma-rays. The two instruments providing data used here for this study are the Magnetic Field Instrument (MFI), which analyzes the solar wind magnetic field parameters and the Solar Wind Experiment (SWE), which gives a wide range of information on the solar wind, e.g. the flow speed of the plasma. For more details see Ogilvie et al. (1995).

3.7   Data hosts / archives

The data of the described missions above are provided by different archives and databases. These are listed in the following table.

Satellite/instrument	Archive/database and link
ACE	ACE Science Center http://www.srl.caltech.edu/ACE/ASC/index.html
ACE and WIND	OMNIWeb Services http://omniweb.gsfc.nasa.gov/
GOES/EPS	Archive of the NOAA National Geophysical Data Center http://www.ngdc.noaa.gov/stp/
SDO/AIA and SDO/HMI	Solar Dynamics Observatory data browser http://sdo.gsfc.nasa.gov/data/aiahmi/
SOHO/EIT	SOHO EIT Catalog http://umbra.nascom.nasa.gov/eit/eit-catalog.html
SOHO/MDI	MDI Data Services & Information http://soi.stanford.edu/data/
STEREO/SECCHI	SECCHI database at US Naval Research Laboratory http://secchi.nrl.navy.mil

Table 3.1. Satellite data archives and databases.

3.8 Solar energetic proton data

The Space Environment Services Center of NOAA provides a list of Solar Proton Events Affecting the Earth Environment (http://umbra.nascom.nasa.gov/SEP/). This list will be referenced as "NOAA proton event list" or short "NOAA list". It contains a total of 252 solar energetic proton events in the time frame from April 1976 to June 2013 (on October 10, 2013) and is based on the integrated 5 minute averages of the proton flux measurements at energies >10 MeV of the GOES satellites. A proton event is defined as such if three consecutive values are at 10 pfu or above. Events that are temporally connected appear as one single event in the list. The list contains information on the time of occurrence and time of proton peak flux, as well as the strength of the associated solar flare and the number of the corresponding active region. Also the first time of observation of the associated CME(s) are noted. This list provides the basis of the analysis of solar energetic proton events in the context of this study due in reference with the NOAA space weather scales.

3.9 GOES / EPS data

The GOES EPS data comprise proton flux measurements for seven energy intervals in the range of 0.6 MeV to 500 MeV and seven categories of integrated proton flux with energy thresholds of 1 MeV, 5 MeV, 10 MeV, 30 MeV, 50 MeV, 60 MeV and 100 MeV. The data consists of integrated 5 minute averages and is provided by the GOES-08, 11 and 13 satellites for the relevant time interval. GOES-11 provides data for the period June 2003 to February 2011. Previous data are from GOES-08, the following data are from GOES-13. Figure 7 shows the proton flux measurements (http://cdaw.gsfc.nasa.gov/CME_list/daily_plots/sephtx/2001_04/sephtx_20010416.png) of GOES-08 for the solar energetic proton event on April 15, 2001. The coloured profiles show the time curve for the proton flux for energy thresholds of 10 MeV, 50 MeV and 100 MeV. Proton flux data are provided as ASCII formatted files. They are not inter-calibrated for the three satellites and differ from spacecraft to spacecraft at the level of a few percent, as can be seen by comparing measurements during overlapping measurement times. While GOES-08 and 11 have one channel for each energy range, GOES-13 has two, one for the eastern and one for the western direction. A comparison of the peak flux values of the two proton channels reveals that the east channel data were used by NOAA for compiling the proton event list. The visual inspection of the GOES-11 data sets revealed missing measurements for an overlapping time period before June 2003. To ensure the data coverage for every event, exclusively GOES-08 data were used during this time period.
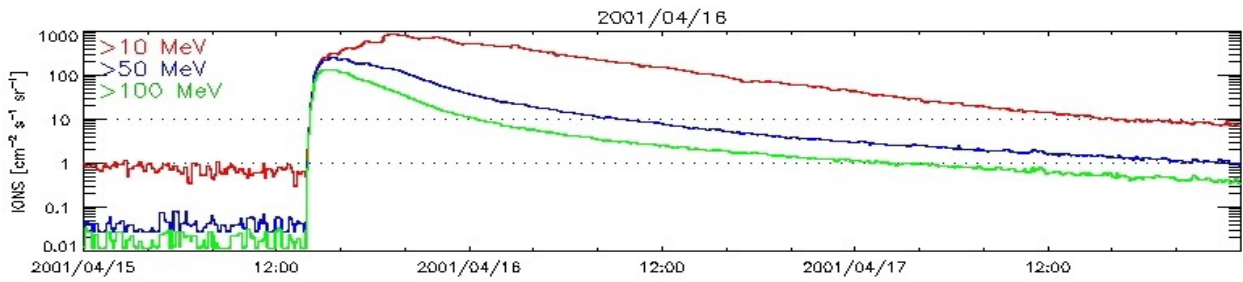
Figure 7. GOES/EPS measurement from April 15 to April 17 in 2001 at energies >10 MeV (red), >50 MeV (blue) and >100 MeV (green). Because of the different particle velocities, the peak flux occurs later for lower energies.

3.10 CME data

Created and maintained by NASA's Coordinated Data Analysis Workshop (CDAW) Data Center and the Catholic University of America, the SOHO LASCO CME Catalogue (http://cdaw.gsfc.nasa.gov/CME_list/). It comprises 20635 CMEs for the period January 1996 to March 2013 (as of October 13, 2013). These CMEs were identified manually using data of the SOHO/LASCO instruments. The CME velocities were obtained from analysis of the SOHO/LASCO C2 and C3 coronagraph data. Because of the nearly loss of SOHO in 1998, the corresponding recovery phase and the ESR mode from December 1998 to January 1999, the catalogue has a gap for these times. The catalogue lists the first time of observation (in UT), three CME velocities (linear, quadratic and quadratic at 20 R_S), the central position angle (Central PA), the measurement position angle (PA), the angular width (AW), the acceleration, the estimated mass and the estimated kinetic energy of a CME. The linear velocity is taken as the average CME velocity inside the LASCO field of view (Gopalswamy et al., 2009).

3.11 Use of solar wind data

Measurements of the solar wind magnetic field components can be provided in different coordinate systems. There are three common geocentric coordinate systems, the geocentric solar equatorial system (GSEQ), the geocentric solar ecliptic system (GSE) and the geocentric solar magnetospheric system (GSM). All three share the origin at the center of the Earth and the X axis, which points at the Sun. For the GSEQ system, the Z axis is perpendicular to the equator of the Earth, while the GSE system's Z axis is perpendicular to the ecliptic plane.

The Z axis of the GSM is the projection of the magnetosphere's dipole axis on the GSE YZ plane (Fränz & Harper, 2002). Data of the magnetic field components Bx, By and Bz of the solar wind are mostly provided in GSE and GSM coordinates. For the investigation of geomagnetic activity the GSM system is most suitable.

The data on the solar wind conditions is provided mainly by the ACE spacecraft with its MAG and SWEPAM instruments. Periods of missing data are covered by data of the WIND/MFI and WIND/SWE instruments. For the time before 2004 this is accompanied by a lower comparability since the WIND spacecraft was not orbiting the Lagrangian point L1 before this time. Figure 8 was retrieved from the OMNIWeb Services and shows a plot of the time evolution of the solar wind magnetic field component Bx and the flow speed. The ACE data has a gap of about two days, which was covered by WIND data. Both the ACE and the WIND data are provided in GSE coordinates and in ASCII formatted files.

While the WIND data used consist of 1 minute averages for both instruments, the ACE/MAG data used consist of 4 minute averages. The ACE/SWEPAM data are averaged over 1 hour.
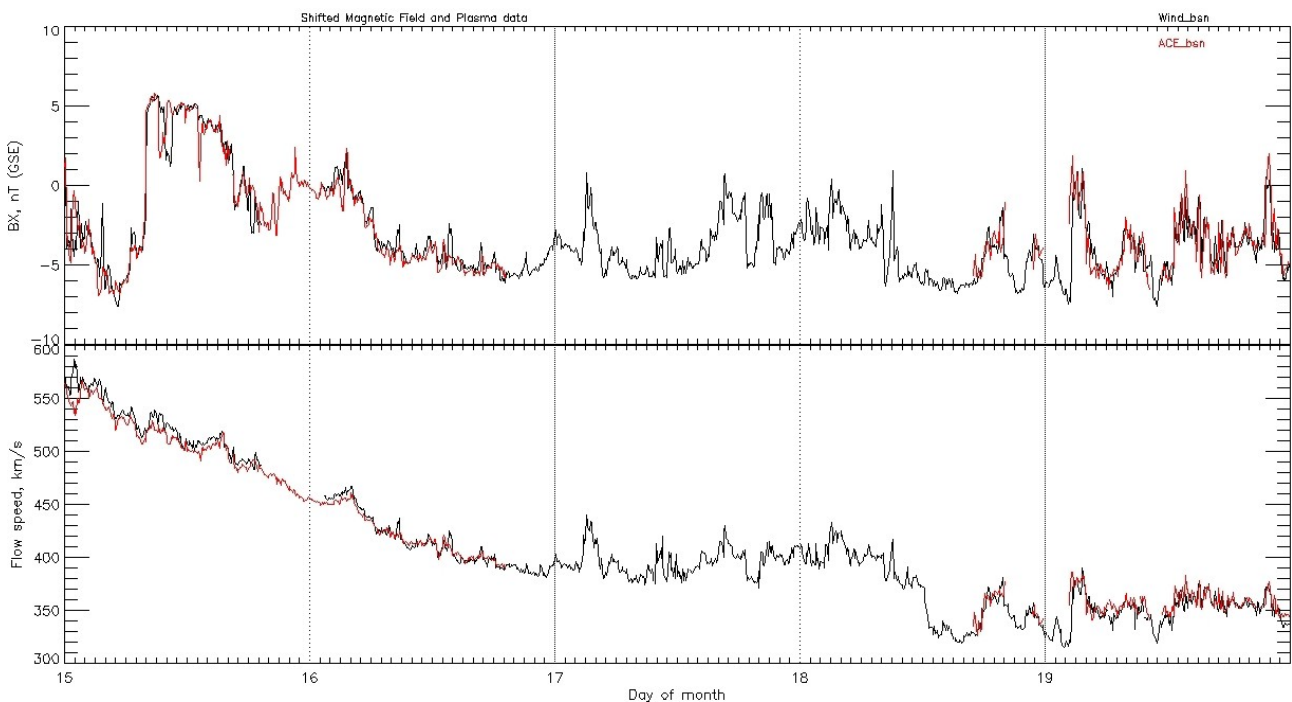
Figure 8. Solar wind measurements for the period February 15, 2000 to February 20, 2000. The upper panel shows the B_x component of the IMF, on the lower panel, the flow speed of the solar wind is displayed. The ACE data is colored in red and the WIND data is black. The ACE data was shifted to the location of the WIND spacecraft. Source: OMNIWeb Services.

3.12 Use of EUV and X-ray data

EUV images of the solar disk at 19.5 nm (Fe XII) from SOHO/EIT and STEREO SECCHI/EUVI and at 19.3nm (Fe XII and Fe XXIV) from SDO/AIA show coronal structures and hot plasma. The observations are used for the detection of EUV flares and coronal holes.

The solar X-ray irradiance measurements provided by GOES/XRS, were used to identify X-ray flares. The data are provided within the GOES plots that are linked to the SOHO LASCO CME Catalog. A sample plot is shown in Figure 9.
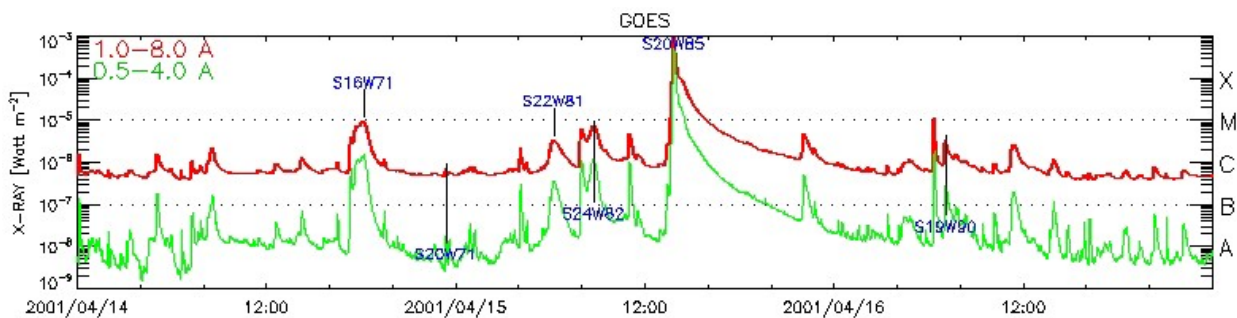
Figure 9. GOES/XRS measurement from April 14, 2001 to April 16, 2001. Spikes of the X-ray flux are from solar flares. The right axis shows the classification of solar flares. Shortly before the onset of the proton event on April 15, an X class flare was detected.

3.13 Solar magnetograms and synoptic charts

Through the Zeeman effect (Zeeman, 1897), the SOHO/MDI and SDO/HMI instruments provide measurements of the solar photospheric magnetic field from which synoptic magnetograms are compiled. These maps are based on the line-of-sight component of the solar photospheric field. The local magnetic field pointing towards the observer/instrument along the LOS is in white. If the magnetic field vector points to the Sun, the area is black. The magnetic flux density is associated with the intensity of the black and white colors. Figure 10 displays a magnetogram that was compiled from SDO/HMI data of November 8, 2011.

After one solar rotation (one Carrington rotation), a magnetogram synoptic chart can be compiled from the central strips of daily magnetograms, showing a magnetic map of the whole solar surface for one rotation. Since the photospheric structures change over time, this map differs from an instantaneous real magnetic field on the solar surface. But for the identification of source regions of solar activity, this difference can be neglected, since the relevant active regions are most likely Earth-faced and therefore within ±90° of the solar disk center. In Figure 11, the SDO/HMI line-of-sight synoptic chart for Carrington rotation 2116 is displayed.
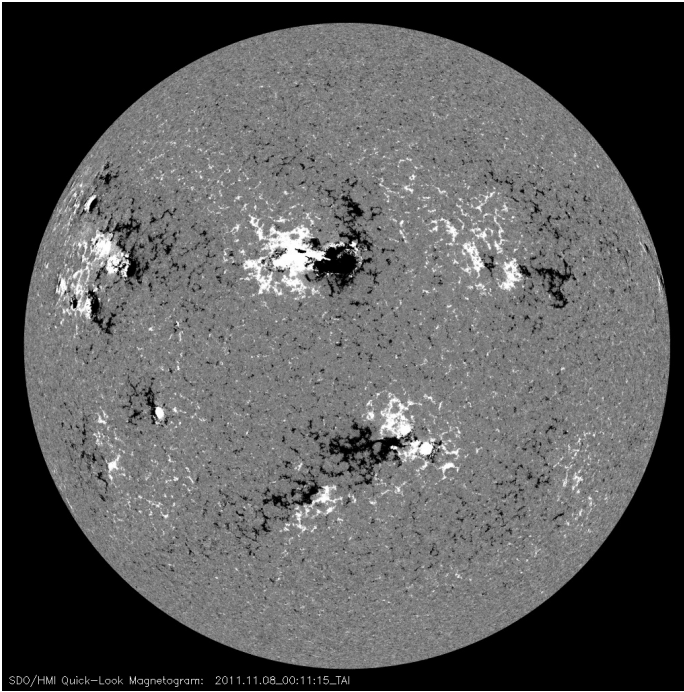
Figure 10. SDO/HMI magnetogram of the solar photospheric line-of-sight magnetic field on November 8, 2011 at 00:04:41 UT. In the white areas the line-of-sight component of the magnetic field vector has positive polarity and points towards the observer, whilst in the black regions, its polarity is negative and points toward the Sun.
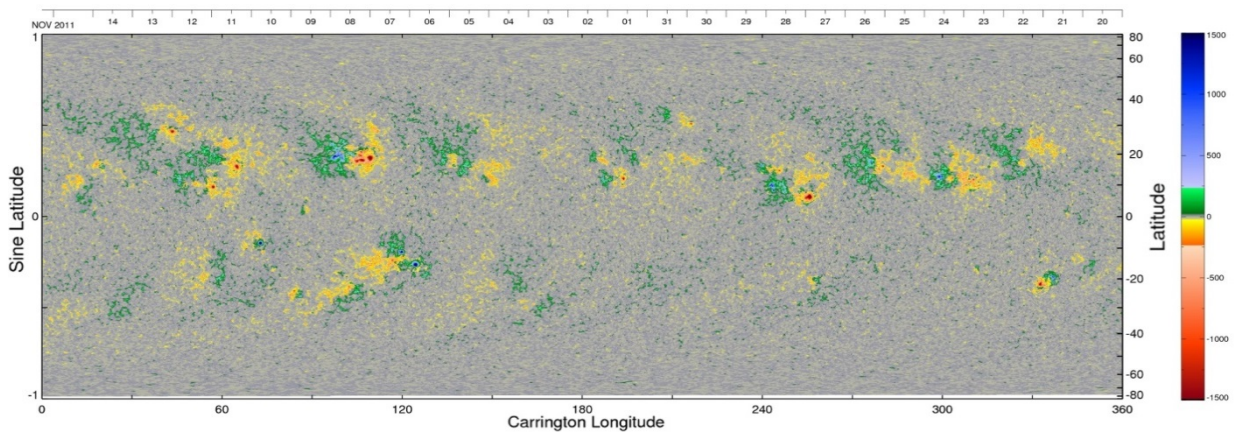
Figure 11. SDO/HMI line-of-sight synoptic chart for Carrington rotation 2116. Regions with inward magnetic field are shown in yellow (low magnetic flux density) and red (higher magnetic flux density), while regions with outward magnetic field are displayed in green (low magnetic flux density) and blue (higher magnetic flux density). Source: http://jsoc.stanford.edu/HMI/LOS_Synoptic_charts.html.

4. Data analysis

This section describes the analysis of the different data sets carried out to help determine the basic properties for each analysed solar proton event.

The Interactive Data Language (IDL), which was developed by ITT Visual Information Solutions for scientific data analysis and visualization, provided the basis for an automated analysis and visualization of the GOES/EPS proton flux data and the ACE/SWEPAM solar wind data. For this study several IDL routines were developed.

4.1 Compilation of the solar proton event list

The NOAA proton event list ranged from 1976 to 2013 at times of this study, but the suitable time frame for the analysis is limited by several factors. One constraint is the necessary requirement of solar wind data at times of an SEP event measured by the ACE satellite at the Lagrangian point $L1$ to help determine the magnetic connection at the onset of the SEP events. Since the ACE spacecraft was launched in 1997, earlier proton events have not been taken into account. The CME velocities are another important source of information required to parametrize the associated solar activity. A time frame limitation for the events arose from the availability of data from the SOHO LASCO CME Catalog which at times of this study comprised the period November 1997 until March 2012, during which the NOAA proton event list contains 105 entries.

The comparison of the solar proton event start times with the CME observation time as taken from the SOHO LASCO CME Catalog, shows that there were periods where no CME information was available due to missing SOHO data. For several CMEs the catalog contained no velocities because the CMEs were too faint or too fast (too few measured points for velocity determination) to obtain reliable velocities. The identification of the associated CMEs is based on coronagraph images and movies taking into account the onset time of the specific solar proton events. The combined investigation of the data, including EUV images, yielded a final solar proton event list containing 81 events and 100 associated CMEs for the time frame under study. Fourteen of these proton events had more than one CME associated with them. These events will be called "multiple events", while the other 67 proton events will be called "single events".

The event list was extended with additional information on the position of the associated solar flares and CME source regions, solar wind conditions and the derived magnetic connection as described in the following sections of this chapter.

The complete event list is provided as screenshot extract in Appendix A1 of this report. The full version is available in xls-format at http://www.affects-fp7.eu/eHeroes-SEPs/.

4.2   Solar source region determination

4.2.1   Coordinate systems

For the spatial information of observed solar features a suitable coordinate system is needed. While x-y coordinates are useful in image processing, they depend on the angular resolution of the instrument they are acquired with. Heliographic coordinate systems as described e.g. by Thompson (2006) use angles for heliographic longitude and latitude. The Stonyhurst heliographic coordinates and the Carrington heliographic coordinates use the same latitudinal angle Θ, but different longitudinal angles Φ (Stonyhurst) and Φ_c (Carrington).

4.2.2   Stonyhurst heliographic coordinates

Devised in the nineteenth century at Stonyhurst College in the UK, Stonyhurst heliographic coordinates are spherical coordinates with the radius $r = R_S$ to describe features on the surface of the Sun. The origin of the coordinate system is at the intersection of the solar equator and the central meridian as observed from Earth. Figure 12 shows a schematic diagram of the Stonyhurst grid on the solar surface. While Stonyhurst heliographic coordinates are static on the solar surface as seen from Earth, Carrington heliographic coordinates rotate with the Sun at a period of the Carrington rotation.
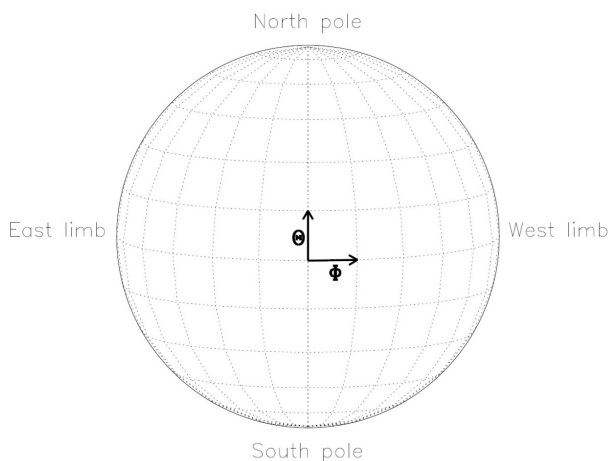
Figure 12. Diagram of Stonyhurst grid from Thompson (2006). Lines of constant heliographic longitude Φ and latitude Θ on the solar disk.

4.2.3 Carrington heliographic coordinates

When observing the solar surface, the Carrington longitude of the central meridian L_0 changes while the Sun rotates. $L_0 = 360°$ for the start of a Carrington rotation and decreasing with time, until it becomes $0°$. Then the next Carrington rotation begins. From L_0 and the observed longitude Φ_C, the Carrington longitude Φ_c can be determined with

$$\Phi_c = \Phi + L_0$$

With the Julian date of the beginning of the first Carrington rotation on November 9, 1853 JD1 and the targeted time JDt of an event, L_0 can be calculated. Dividing the time difference of these two Julian dates by the period of the Carrington rotation gives the corresponding Carrington number and a residual time. The Sun rotates at $360°$ per ≈ 27.28 d, which is a rotation rate of approximately $13.2°$/day. Multiplying the residual time and the rotation rate leads to L_0, so that the Carrington longitude Φc is given by

$$\Phi_c \quad = \Phi + L_0 = \Phi + [360° - ((\text{JDt} - \text{JD1}) \bmod 27.28) \text{ d} \cdot 13.2°/\text{d}]$$

Note that the content of the square brackets is always between $0°$ and $360°$ and rises with the rotation of the Sun towards the end of a Carrington rotation. At the beginning of a Carrington rotation both heliographic coordinate systems overlap.

4.3 Identification of CME source regions

The flare regions for the events of the list were identified with the program *jhelioviewer* (http://jhelioviewer.org/linux.html), using EUV images and movies of 19.3 nm and 19.5 nm wavelengths at the resolution of 2000×2000 arcsec, providing x-y coordinates of the flare positions. These were displayed by the program when pointing the cursor at a designated position and due to the size of the cursor, a reading error of ± 30 arcsec was assumed. With the approximate positions of the particular active regions, the CME source regions were then identified on magnetograms and further on in the synoptic charts. From those the Carrington coordinates of the source regions were obtained. Assuming an reading error of ± 5° for longitude and latitude, the position of the most intense positive and the most intense negative magnetic flux density of the source region were identified, yielding the approximate size of the source region core.

With the Carrington coordinates and the corresponding Carrington number of each synoptic chart, the positions were determined from the event time information.

For visualization purposes, Stonyhurst heliographic coordinates are most suitable. Using the above relation, with the IDL routine *coord_trans.pro* the Carrington coordinates were read from the compiled event list and transformed into Stonyhurst coordinates, which were written into an output file. This method for the source region determination is similar to the method of Tripathi et al. (2004) but instead of neutral lines the positions of the most intense flux densities were identified to estimate the core size of the source regions.

4.4   Analysis of GOES / EPS data

The peak flux values and onset times of the proton events are provided through the NOAA proton event list. Beyond this information, the event duration time is an important parameter for the analysis of radiation impacts. It was assumed that the full width at half maximum (FWHM) approach applied to the individual flux profiles might be a parameter for proton event comparison. In order to automatically analyze the GOES/EPS data, the IDL routine *goes_analysis.pro* was developed. For the analysis of the proton flux data, the year, month and day/time of the proton event onset provided by the NOAA list were written to a data file. The Carrington heliographic coordinates, the speed of the associated CME and the event type (single or multiple event) have been added. The onset times for every event were transformed into reduced Julian Date (reduced JD) and the Carrington coordinates were transformed into Stonyhurst coordinates. Then, for each event, the IDL routine searched the current directory and its sub-directories for GOES/EPS proton flux data sets and read out those data sets for which the names matched the time frame containing the onset time of the proton event. Because the period covered by GOES-11 is the longest in time, the routine prefers to take GOES-11 rather than GOES-13 data for the overlap time period. The data sets were read into an array and the time stamps were also transformed into the reduced JD format. The exact time of the event onset was determined by comparing the event onset time from the NOAA list with the time stamps of this data set. If a match was found, it is taken as the starting time for the analysis. If no match was found, the data set was searched for the beginning of the event. The program took the time stamp closest to the values of the NOAA list and searched for the first three proton flux values that were equal to 10 or larger. An additional requirement for the event onset definition was that the values before the designated event onset point were lower than 10 pfu. The event end is defined as the time when the flux value dropped below 10 pfu. The IDL routine calculates then the event duration from the event start and end times and determines the maximum intensity in between.

For the FWHM, the time between event onset and maximum, as well as the time between the intensity maximum and event end were identified for the proton flux values that were closest to the half maximum value. For the radiation dose analysis the particle flux was summed over the event duration to derive the total particle counts.

The results were written into an output file and then plotted as a function of the CME speed and the Stonyhurst longitude. Additionally, the total particle count was plotted as a function of event duration and peak flux, while the peak flux was also plotted as a function of the event duration.

It turned out that the FWHM of a solar proton event is practically very difficult to obtain through automated analysis of the proton event profiles, as shown in Figure 13 for the single proton event on November 7, 2004. Several peaks were higher than the half value of the peak flux, which made it impossible to determine a reasonable FWHM value. For 46 of the 81 proton events, the FWHM determination was not feasible, so the use of the FWHM as parameter to compare the proton events was finally discarded.

Figure 13. Solar proton event of November 7, 2004. The peak flux of the single event is 495 pfu. The FWHM cannot be determined reasonably due to several peaks that are higher than half of the maximum value.

4.4.1   Inter-calibration of GOES data

As stated earlier, the GOES/EPS data are not provided inter-calibrated. For this purpose the *goes_intercalibration.pro* routine was developed, creating the least-squares method to determine an offset value and a scaling factor. The input parameters were the numbers of the two GOES satellites which data were analyzed for inter-calibration. The program searches for overlapping data files and reads the proton flux values and the time stamps, which were then transformed into reduced Julian Day for comparison. The data were filtered for missing values and non-matching Julian Dates. An inter-calibration attempt was performed for GOES-08 and GOES-11 before exclusion of the overlapping GOES-11 data showing that these data sets are similar with an offset value of ≈ 0.1 pfu. The scaling factor was very close to 1 with a variation of the order 10^{-3}. Hence, explicit inter-calibration of the different data sets is not required for the exactness level needed for this study. The GOES-11 and 13 data overlap from April 2010 to February 2011, a period during which only one proton event with a very low peak flux of 15 pfu was detected. Therefore the inter-calibration based on these data is not reasonable since the data contain mostly noise with only six small peaks, one at 15 pfu and five between 1 and 6 pfu. The *goes_analysis.pro* routine is also capable to analyze random proton flux data to detect solar proton events. The only change in the program code for this purpose would be to enable the independent data file selection and allowing the routine to freely search for the onset of a solar proton event for a given time period. The analysis of GOES/EPS proton flux data for energies >100 MeV and the inter-calibration of the data sets could be performed after minor changes to the code. For the inter-calibration of future data however, reliable parameters and therefore overlapping data sets including data on several solar proton events would be required.

4.5   3D magnetic connection to the Sun

As pointed out earlier, the propagation of solar energetic protons in interplanetary space depends on the conditions of the background solar wind. With the flow speed of the solar wind and the *Bx* (GSE) component of the IMF, the sources of the solar wind can be identified and the three-dimensional magnetic connection to the Sun can be obtained.

The solar wind data for the time period under study were provided in ASCII-format, for which an IDL routine was developed to determine the solar wind flow speed and IMF *Bx* values for the proton events. ACE/SWEPAM did not provide data before February 5, 1998, so for the first two proton events of the list since the launch of ACE, data provided by the WIND spacecraft were used.

The routine *ace_solarwind.pro* reads the start times from the provided list and transforms them into reduced JD format. Then the ACE/MAG and ACE/SWEPAM data sets, which include only the B_x values and flow speeds, were read for the whole time frame under consideration. The time stamps of both data sets were also transformed to reduce JD to optimize the search for matching times. Values such as -9999, indicating data gaps were replaced by a NAN (not a number) markers, so that they do not influence the plotting ranges. The solar wind flow speed was taken from 1 hour before the onset time of the solar proton event because the solar wind needs additional time to travel from the Lagrangian point L1 to Earth, where the protons were measured by the GOES satellites. B_x and the flow speed were then plotted for each event into postscript files. For good readability, B_x was plotted over a time period of 7 days, so that short time scale variations do not interfere. The solar wind flow speed was plotted for a period of 40 days, so that more than one complete solar rotation (27.28 d) could be displayed and recurring features could be identified. Figure 14 shows these plots for the proton event on May 7, 2001.
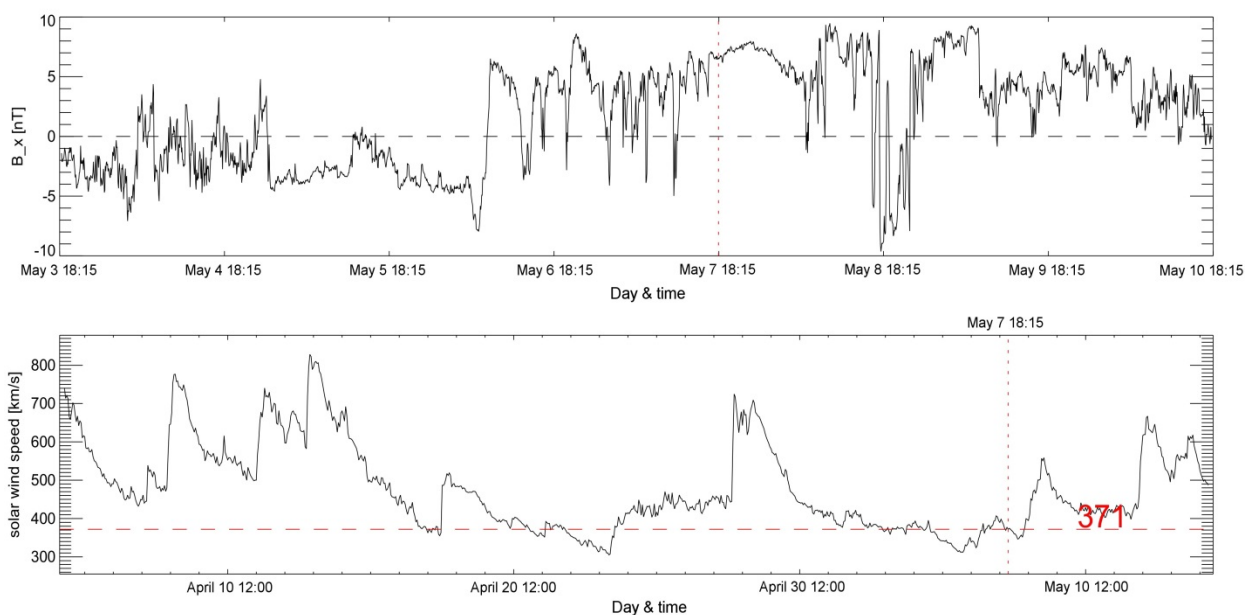
Figure 14. Solar wind conditions for the proton event on May 7, 2001. The upper plot shows the B_x component of the IMF for a period of 7 days. The B_x value is positive at the onset of the proton event, which corresponds to a negative polarity of the IMF. The dashed line marks the zero level. The solar wind speed plot (lower panel, for a period April 4 - May 14, 2001) contains a horizontal line at the value of the determined flow speed at proton event onset. In this case the onset occurred at a flow speed of 371 km/s. The red, vertical broken line marks the time at one hour before the onset of the proton event.

The direction of B_x (GSE) was identified this way for all events. For positive values of the B_x component the IMF is negative and for negative B_x it is positive, since B_x points towards the Sun. Plots of WIND/MFI data from OMNIWeb were used for 5 events in which no ACE/MAG data were available.

Assuming a constant solar wind flow speed, the approximate ejection time of this particular solar wind was calculated using the distance between the Sun and the Lagrangian point $L1$, which is $\approx 1.485\ 108$ km (0.99 AU) for the semi-major axis. The Sun rotates at $\approx 13.2°$/day and with the travel time of the solar wind, the heliographic longitude of the solar wind source at the onset of the solar proton event was estimated. For identification of the latitude of the solar wind source regions, EUV 19.5 nm images and magnetograms with a 10°- grid provided by Solar Monitor (solarmonitor.org) were analysed. Due to the spatial extension of the coronal structures identified, an uncertainty of ±10° for the latitudinal and longitudinal angles was assumed. Figure 15 shows the SOHO/EIT 19.5 nm image and MDI magnetogram for May 3, 2001. For best visibility of the solar wind sources, images near the estimated ejection time of the solar wind were investigated. In this case the solar wind source region was identified as dark, open area in the EUV image, circled orange.
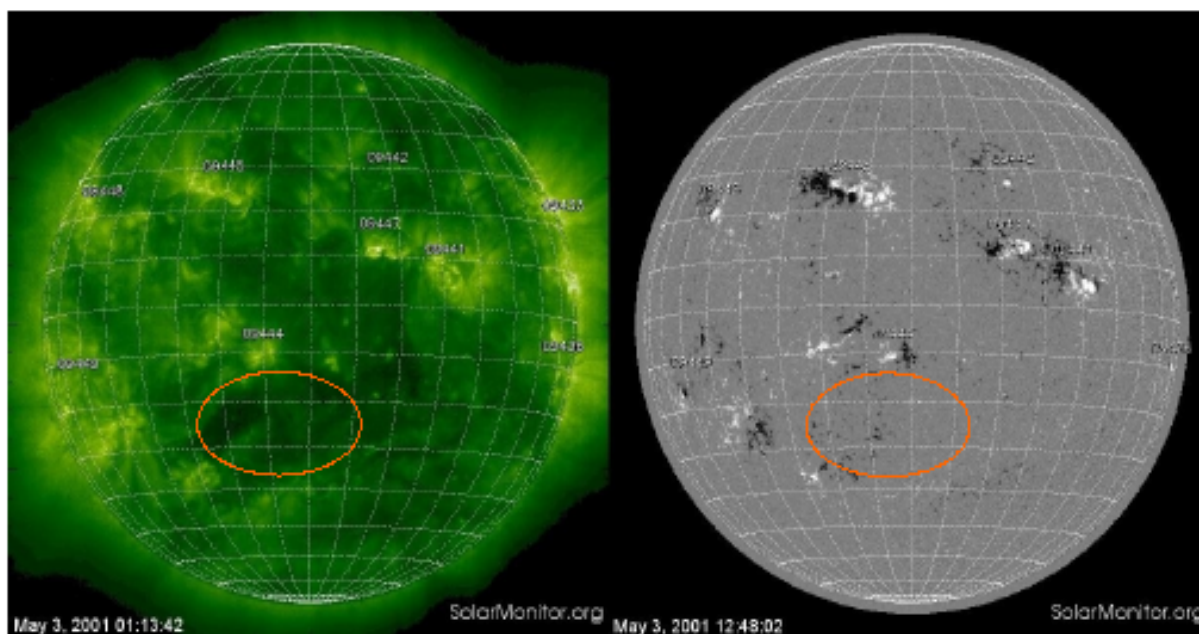
Figure 15. SOHO/EIT 19.5 nm image (left) and SOHO/MDI magnetogram (right) taken on May 3, 2001. The identified source region of the solar wind for the proton event in May 2001 is circled orange at a latitude of about -25°. Fast solar wind was measured about one day after the onset of the solar proton event. The right panel shows slightly more black dots in the marked region, which agrees with the negative polarity obtained from the B_x plot in Figure 14.

Since the EUV radiation imaged e.g. by SOHO/EIT is emitted by hot plasma in the solar corona, dark structures in those images indicate the presence of coronal holes which are the sources of fast solar wind. Here slow wind is estimated to originate from regions nearby and westward of the identified coronal hole.

To estimate the angular distance between the identified solar wind source regions and the identified source region of the CME that were associated with an individual proton event, the great-circle distance α on the solar surface was calculated. With Θ_1 and Φ_1 being the heliographic latitude and longitude of the proton event source region and Θ_2 and Φ_2 being the heliographic latitude and longitude for the source region of magnetic connection, α is given by $\alpha = \arccos (\sin \Theta_1 \sin \Theta_2 + \cos \Theta_1 \cos \Theta_2 \cos(\Phi_1 - \Phi_2))$.

For the calculations, the proton event source region coordinates closest to the tentative source region of magnetic connection were taken.

The distance from Sun to Mars varies between 1.381 AU and 1.666 AU, with a semi-major axis of 1.524 AU. For the following considerations it will be approximated to 1.5 AU. Let γ be the angle between two arms of the Parker spiral. Between these two spiral arms the solar wind speed is assumed to be constant. The distance of the crossing points of the spiral arms are then a_E at Earth orbit and a_M at Mars orbit. The linear distance between the Sun and the crossing points of the spiral arms at the two orbits are the radii of the orbits $r_E = 1$ AU and $r_M = 1.5$ AU. So in 2D it is $\sin (\gamma/2) = a_E/2 \, (r_E)^{-1} = a_M/2 \, (r_M)^{-1}$ i.e. $a_M/a_E = r_M/r_E$.

Thus, the widening of the spiral depends only on the distance from the Sun if the solar wind velocity is equal for the spiral arms. For different solar wind velocities however, the velocity differences cause distortion of the spiral structure. The magnetic connection is given by the IMF which also changes with the expansion the Parker spiral. The magnetic flux density decreases as r^{-3} for the magnetic dipole field of the Sun, but due to multipole components of the magnetic field caused by the moving plasma, the decrease is slower. Analogous to the geometrical widening of the spiral, the duration of the magnetic connection at Mars orbit is also 1.5 times longer than at Earth orbit, assuming a constant solar wind flow speed.

5. Results

5.1 Statistics

5.1.1 Solar radiation storms

The NOAA proton event list contains 252 solar proton events for the time period from April 1976 to September 2013. 81 of them occurred in the time period November 1997 to March 2012 for which ACE and WIND solar wind data were available. These events have been analysed in this study. Table 5.1 lists the solar proton events for both time periods and provides information on the number of solar radiation storms in the categories of the NOAA space weather scales. Note that no extreme solar radiation storm was detected in the whole period. The strongest storms detected were in the "severe" category.

Time frame	total	minor	moderate	strong	severe
Apr. 1976 – Sep. 2013 percentage of total events	252	145 57.5%	68 27.0%	30 11.9%	9 3.6%
Nov 1997 - Mar 2012 (total) percentage of total events	105	58 55.2%	28 26.7%	13 12.4%	6 5.7%
Nov 1997 - Mar 2012 (analyzed) percentage of total events	81	43 53.1%	22 27.2%	10 12.3%	6 7.4%

Table 5.1 Numbers of solar radiation storms from the NOAA proton event list. Top row: time period of full NOAA list, middle row: time period for this study, bottom row: percentages. Note that, no extreme (R5) solar radiation storm occurred during the whole time frame covered by the list.

The full period covers 3.5 solar cycles, including 4 solar maxima, while the period analysed covers 1.5 solar cycles with nearly 2 solar maxima. Figure 16 shows a composite plot of the full proton event list together with the sunspot number. Frequency peaks seem to occur at or close to the beginning of a sunspot cycle and in its declining phase, giving rise to a kind of double peak nature of the time frequency distribution. Some events, like in 1986 do occur even at times of solar activity minimum. A proper interpretation likely requires analysis of the coronal structures at these times and the occurrences of active regions. During the solar maximum in 2000 to 2002, 54 solar proton events were detected, more than half of the events of the time period of the studied interval between November 1997 and March 2012. Note, that from January 2007 until July 2010 (last solar minimum) no solar proton event was measured and that the last minimum and present maximum phases showed very low sunspot numbers.
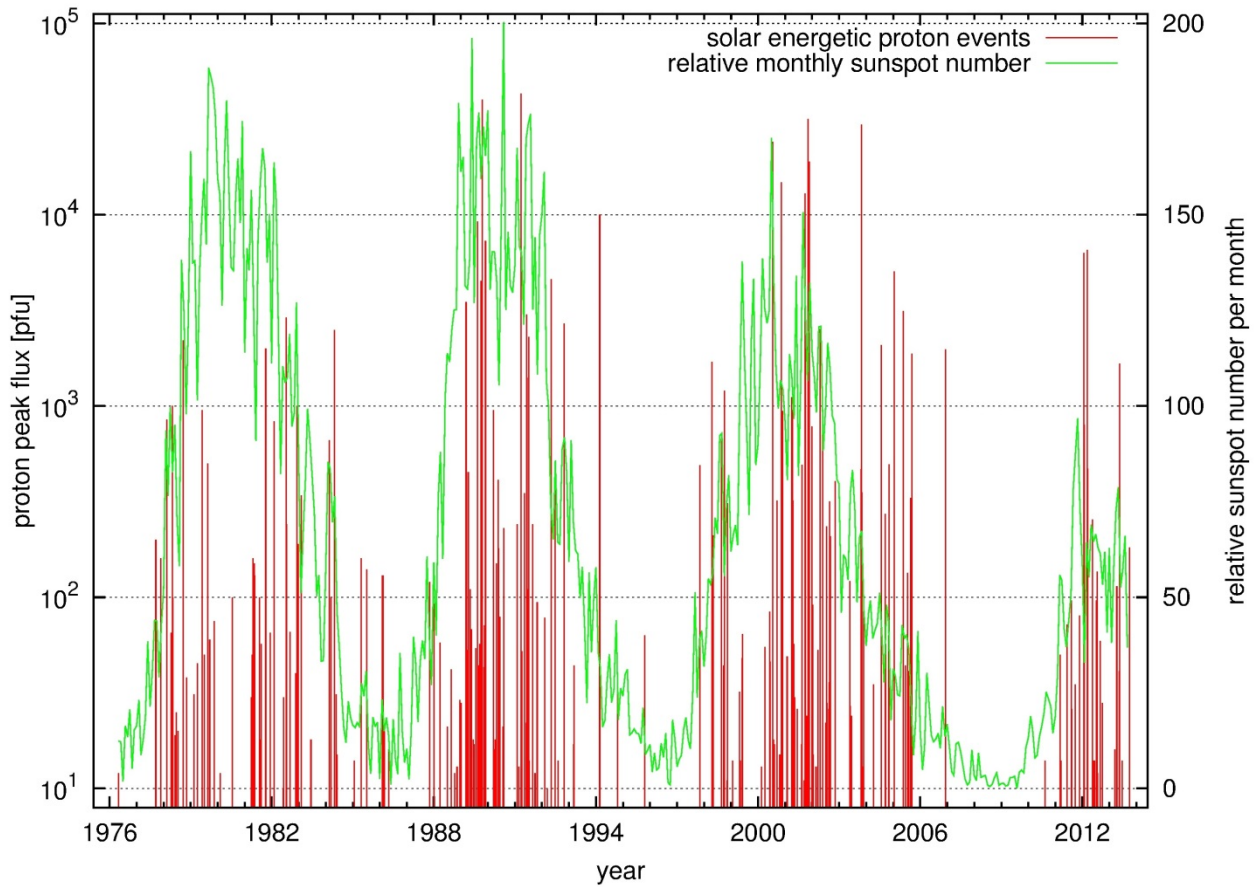
Figure 16. Plot showing the NOAA solar proton events (red) together with the relative sunspot number per month (green) from 1976 until 2013.

5.1.2 Proton associated CME speeds

For the period from January 1996 to March 2013, the SOHO LASCO CME catalogue (http://cdaw.gsfc.nasa.gov/CME_list/) provides information on a total of 20635 CMEs. Figure 17 shows the CME speed distribution derived from the catalogue data. If one takes 750 km/s for comparison, being typical for fast solar wind from coronal holes, one finds that only 1631 ($\approx$ 7.9%) of the CMEs were faster.
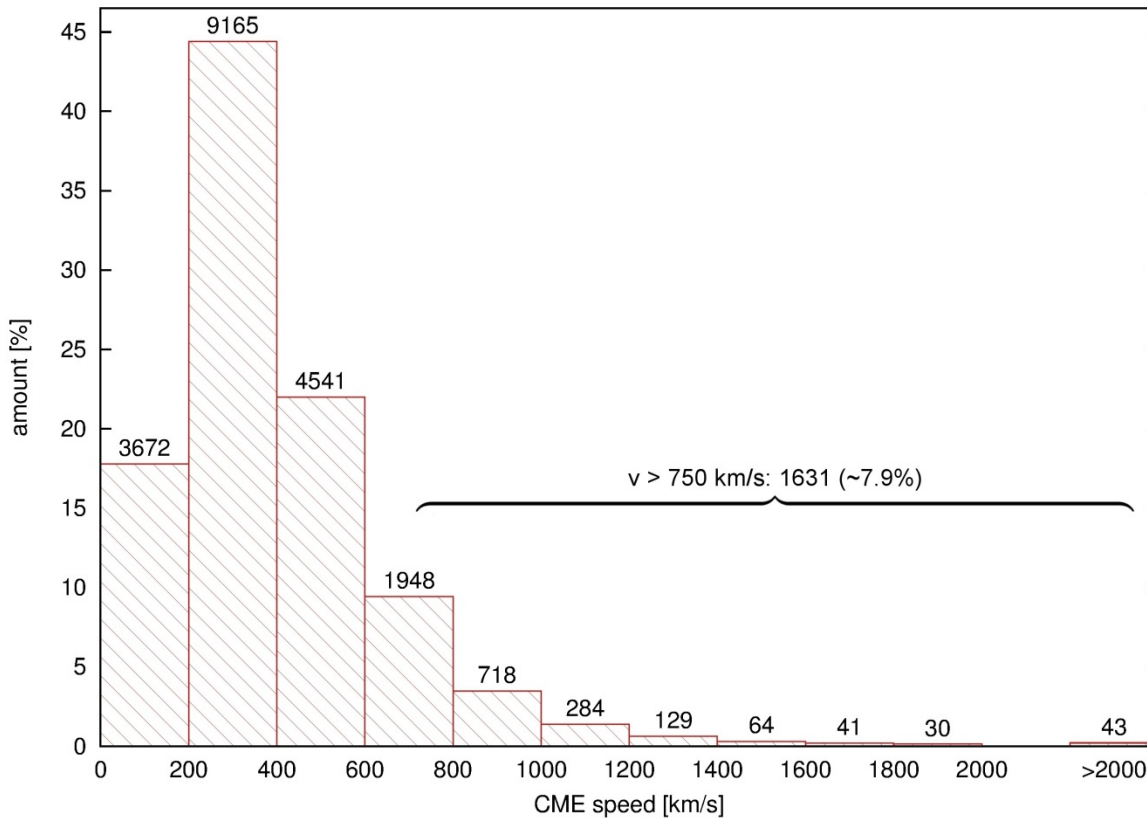
Figure 17. Speed distribution for the 20635 CMEs of the SOHO LASCO CME catalogue for the time period January 1996 until March 2013. 1631 CMEs ($\approx$ 7.9%) had a velocity greater 750 km/s.

For the SOHO LASCO CME catalogue, the CME velocities are determined through height-time measurements using LASCO C2 and C3 observations (Gopalswamy et al., 2009). Since single-point observations are used, for geometrical reasons the accuracy of this method is sensitive to the direction of the CME. For CMEs that are observed at the limb of the solar disk, i.e. at 90° with respect to the line-of-sight of the observer the CME speed error should be small, whereas for other CMEs the error would be larger. The LASCO CME speeds of the catalogue are affected by these uncertainties but it is beyond the subject of this study to address this issue in more detail.

In the time frame November 1997 to March 2012, during which 105 solar proton events were analysed, a quick comparison with the CME catalogue yields, that 81 of them could be asssociated with 100 CMEs, including multiple particle events. The speed distribution of these 100 CMEs is shown in Figure 18. 98 CMEs had a velocity greater 750 km/s, one was right at 750 km/s and only one CME was slower. It is obvious that intense SEP events are associated with fast shock CMEs driving shock waves, being indicative of shock acceleration as source of the particles as found by e.g., Reames et al. (1997). This is supported by the fact that in four cases the CMEs were associated with erupting filaments only but not with X-ray flares.
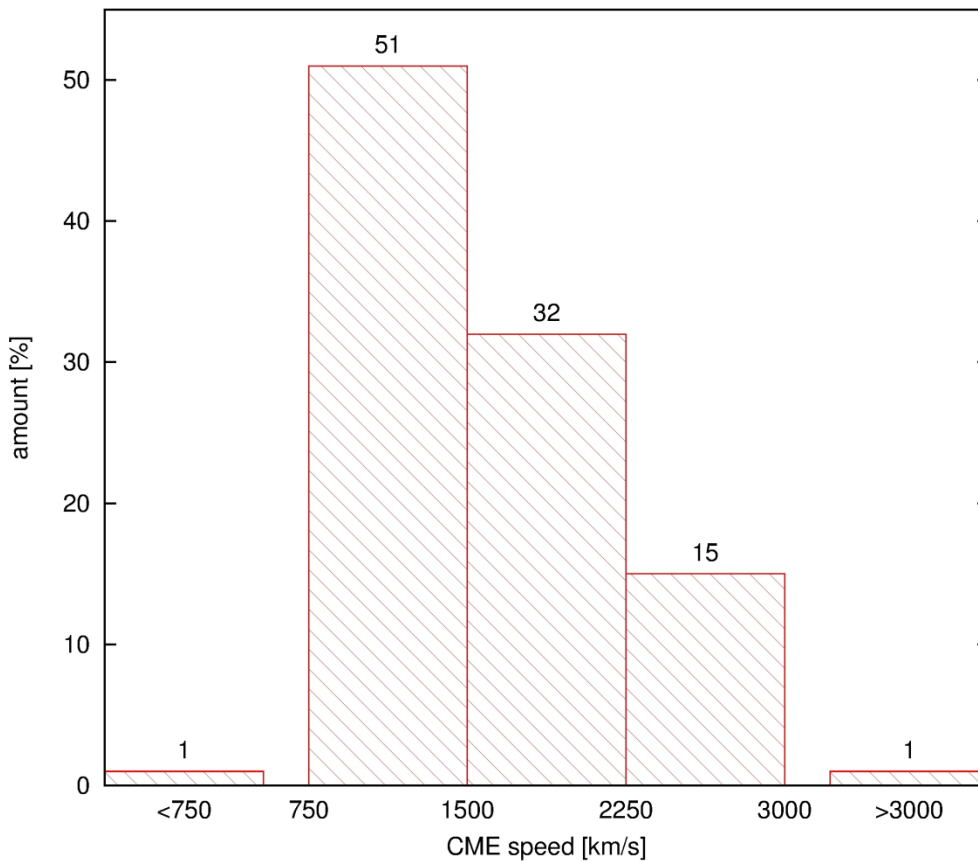
Figure 18. Speed distribution for the 100 CMEs that were associated with the 81 single and multiple solar proton events during the time period November 1997 to March 2012. 98 CMEs had a velocity greater 750 km/s, one was right at 750 km/s and only one CME was slower.

5.1.3   Single and multiple particle event types

For subsequent analysis the categorisation of the proton events into "single events" and "multiple events" as shown in Figure 19 is important because in "multiple events" having more than one CME associated with them the derived proton event parameters cannot be uniquely correlated with the CME parameters. Therefore, the following analyses of proton events in relation to the CME speed or the CME source region positions will only contain the 67 identified "single events" from the NOAA proton list, while the analysis related to the event duration and the total measured protons per event will involve all 81 proton events.
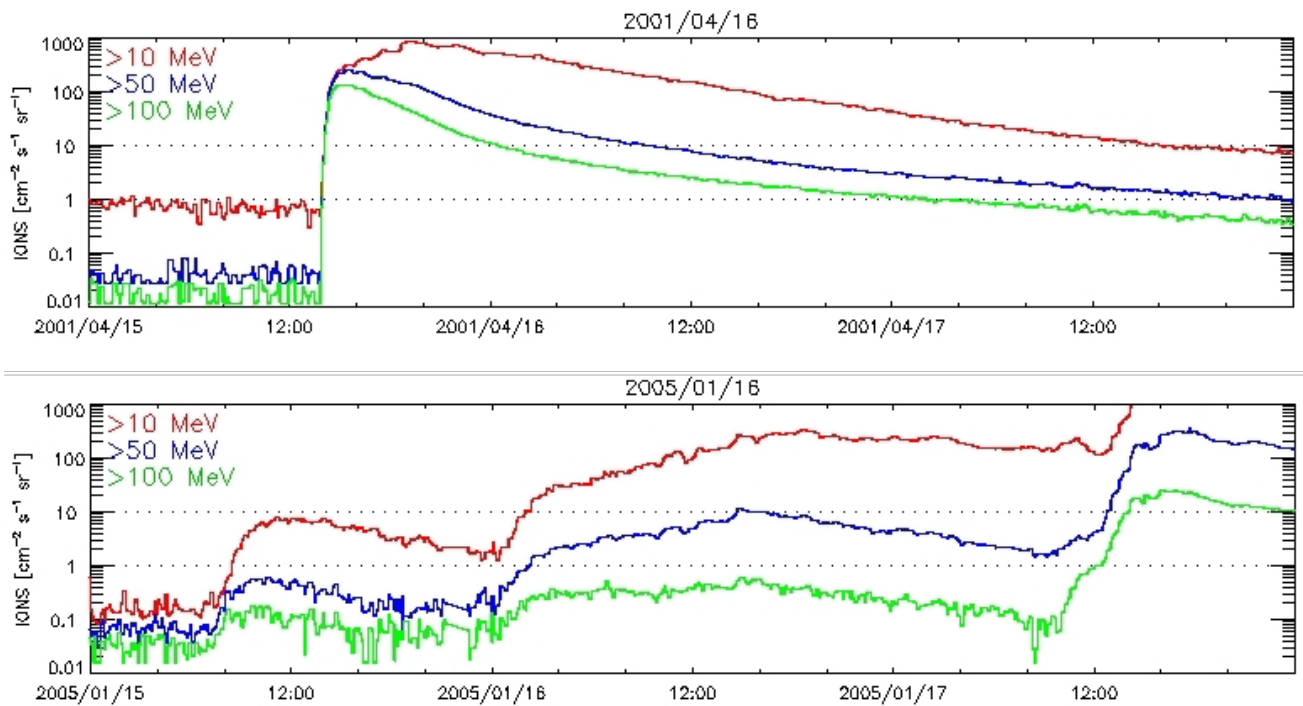
Figure 19. GOES/EPS proton flux for energy thresholds of 10 MeV, 50 MeV and 100 MeV. The upper image shows the proton flux data of the "single event" on April 15, 2001. The lower one shows the proton flux of the "multiple event" on January 16, 2005. Note that the proton flux peak on January 15 does not reach the threshold of 10 pfu and is therefore not considered a proton event. The proton event starting on January 16 is superimposed by another event on January 17. Sources: PTHX plots from the SOHO LASCO CME catalogue.

5.1.4　CME source regions

The source regions of the associated CMEs were identified using the positions of the related solar flares in observations of the SOHO/EIT telescope at 195 Å. Since four CMEs came from erupting filaments, their source regions are not contained in the plot. Figure 20 shows the solar flare positions on the solar disk. While the distribution of the positions appears similar for the northern and southern hemispheres, the number of the proton event source regions is significantly higher in the western hemisphere as expected from the magnetic connection along the nominal solar wind spiral.
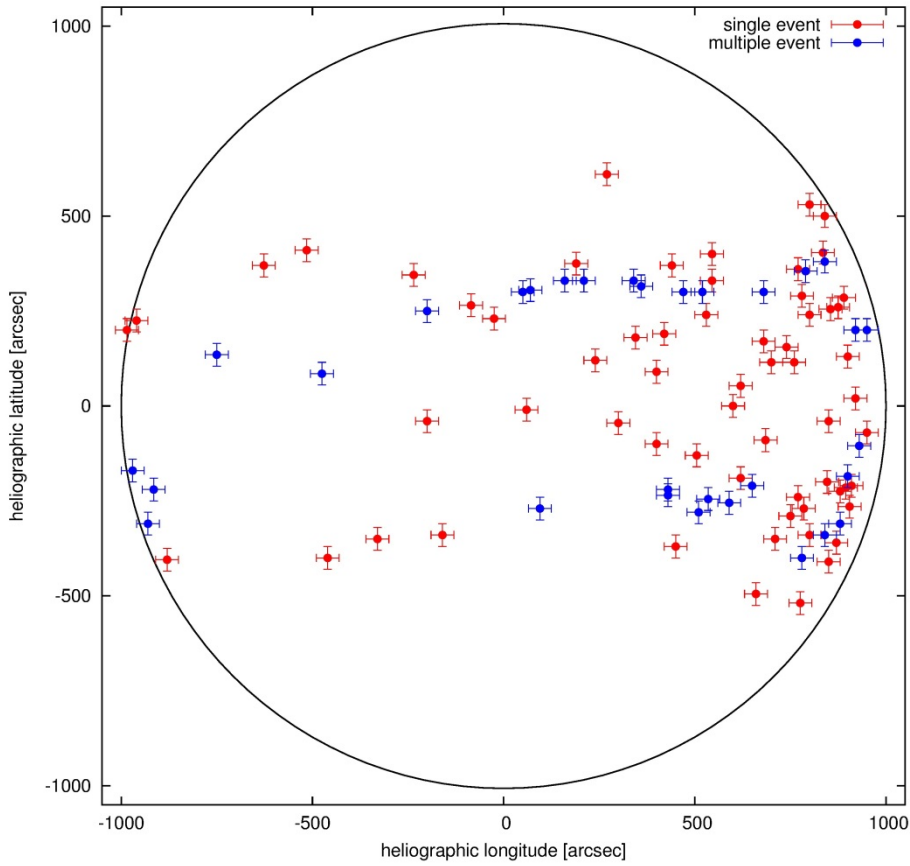
Figure 20. Flare positions on the solar disk for the proton events, as identified from SOHO/EIT 195 A images Single proton events are labelled red, multiple proton events are labelled blue).
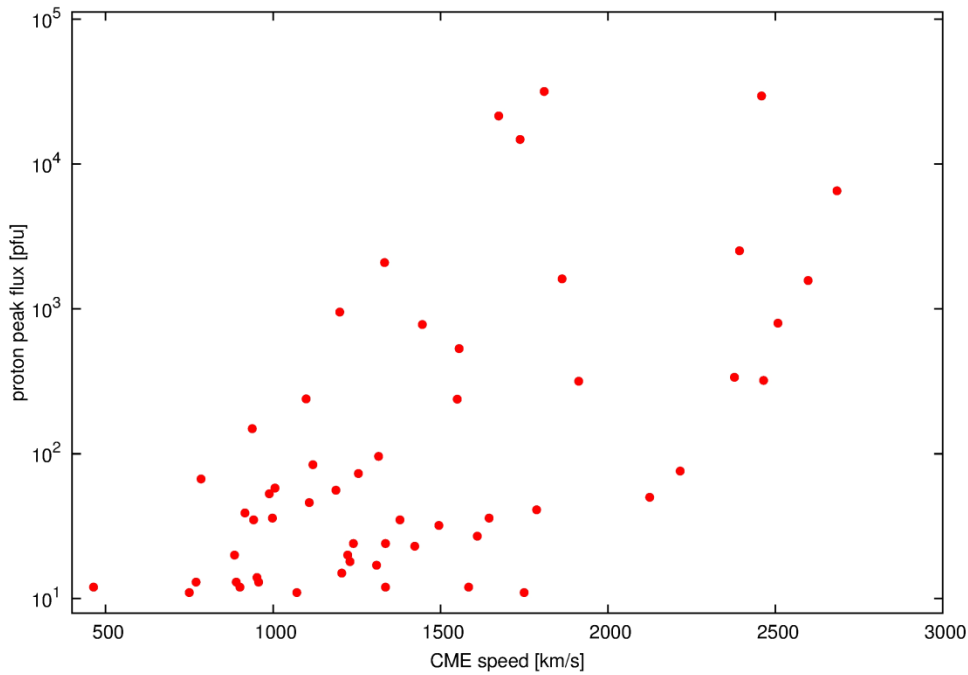
Figure 21. Logarithmic plot of the proton peak flux as a function of CME speed.

Figure 21 shows the proton peak flux in the individual proton events plotted as a function of the associated CME speed in the SOHO/LASCO field of view. The lowest associated CME speed was 464 km/s, associated with a proton peak flux of 12 pfu, which is just above the threshold for proton event detection. All other CMEs had velocities of 750 km/s or above. In general, the peak flux rises with increasing CME speed as shown by Kahler & Vourlidas (2013). But there are also very fast CMEs with $v > 2000$ km/s that produced proton events with peak fluxes below 1000 or even 100 pfu. Different from the analysis of Kahler & Vourlidas (2013), who limited CME source region longitudes to distances >40° in the western hemisphere of the Sun with respect to central meridian, to minimise CME projection effects, in this study all source region longitudes are considered. It shall be noted that CME speeds are used in this study only as proxies for the CME driven shock speeds which should be faster (e.g., Möstl et al. 2012).

5.1.5   Intense solar proton events

According to the NOAA scale, six severe and ten strong solar radiation storms could be analyzed for the time period of this study. Table 5.2 provides an overview on the basic parameters of these sixteen events and the speeds of the associated CMEs.

Date	peak flux [pfu]	duration [d]	total protons	CME speed [km/s]
Nov 4, 2001	31700	4.78	$8.41 \cdot 10^5$	1810
Oct 28, 2003	29500	3.38	$1.09 \cdot 10^6$	2459
Jul 14, 2000	21500	5.29	$3.99 \cdot 10^6$	1674 multiple event
Nov 22, 2001	18900	3.95	$5.44 \cdot 10^5$	1738
Nov 8, 2000	14800	2.47	$2.85 \cdot 10^6$	2402
Sep 24, 2001	12900	5.84	$3.37 \cdot 10^5$	
Mar 7, 2012	6530	5.58	$1.93 \cdot 10^5$	2684
Jan 23, 2012	6314	4.14	$3.09 \cdot 10^5$	2175 multiple event
Jan 16, 2005	5040	6.59	$1.45 \cdot 10^5$	multiple event
May 14, 2005	3140	1.05	$9.32 \cdot 10^4$	2393 multiple event
Apr 21, 2002	2520	4.48	$1.68 \cdot 10^5$	1333
Oct 1, 2001	2360	3.43	$7.29 \cdot 10^4$	1863
Jul 25, 2004	2090	1.67	$2.18 \cdot 10^4$	2598 multiple event
Apr 20, 1998	1610	4.00	$4.27 \cdot 10^5$	
Nov 2, 2003	1570	2.36	$1.61 \cdot 10^5$	
Apr 2, 2001	1110	3.56	$1.71 \cdot 10^5$	

Table 5.2 Proton event parameters and speeds of the associated CMEs for the ten strong and six severe radiation storms during Nov. 1997 to Mar. 2012. The proton events are sorted with respect to their peak flux values.

Five of the severe solar radiation storms occurred during the solar maximum 2000 to 2002. Another one was detected in October 2003, i.e. in the declining phase of the solar activity cycle. Of the strong events, one was measured in 1998 when solar activity was rising, three took place during the solar maximum of 2000 to 2002, four occurred between this maximum and the following minimum, and finally two strong events were measured during the last solar maximum in 2012. Five events were multiple events, for the other eleven, the comparison of the CMEs speeds showed that all associated CMEs were faster than 1300 km/s, six of them were even faster than 2000 km/s. Considering the peak flux values, there does not seem to be a simple direct correlation with the CME speeds.

The time duration of the proton events lasts from about 1 day for the multiple event on May 14, 2005 to about 6.6 days for the multiple event on January 16, 2005. An interesting outcome is that single events also have durations of up to about 5.3 days. Since it is likely to assume that the energetic protons are accelerated at the shock that is driven by the CME, the proton event is thought of as to end in time after the shock has passed Earth. The long durations for single events suggest that particles are accelerated by the CME driven shock further out in the heliosphere. The number of total protons that were measured during the events is of the order of 10^4 to 10^5 for strong events and 10^5 to 10^6 for severe events. A possible correlation between the total measured protons and the peak flux values or the event duration will be discussed in following sections.

5.2   Magnetic connection to the CME source regions

5.2.1   Solar wind speed, IMF polarity and magnetic connection to source regions

The plots created by the *ace_solarwind.pro* routine provided the solar wind flow speed for 65 proton events from which the solar wind speed and type at event onset were derived as input to calculate the spiral connection to the Sun in solar longitude. The plots were also used to derive the B_x-component as indicator of the solar wind's IMF polarity. This was possible in 54 proton events, whereas in 15 multiple changes of the B_x direction occurred within several hours as being indicative of complex solar wind flows typical around times of maximum solar activity and proximity to heliospheric current sheets. For four events no ACE/SWEPAM data were available and the solar wind flow speed was taken from WIND/SWE measurements. The visual inspection of the solar wind data at times of the proton events revealed that twelve proton events were observed shortly after passage of an interplanetary shock (Figure 22, the shock can be identified through the sudden changes of the plasma parameters as described e.g. by Bemporad & Mancuso (2010)).
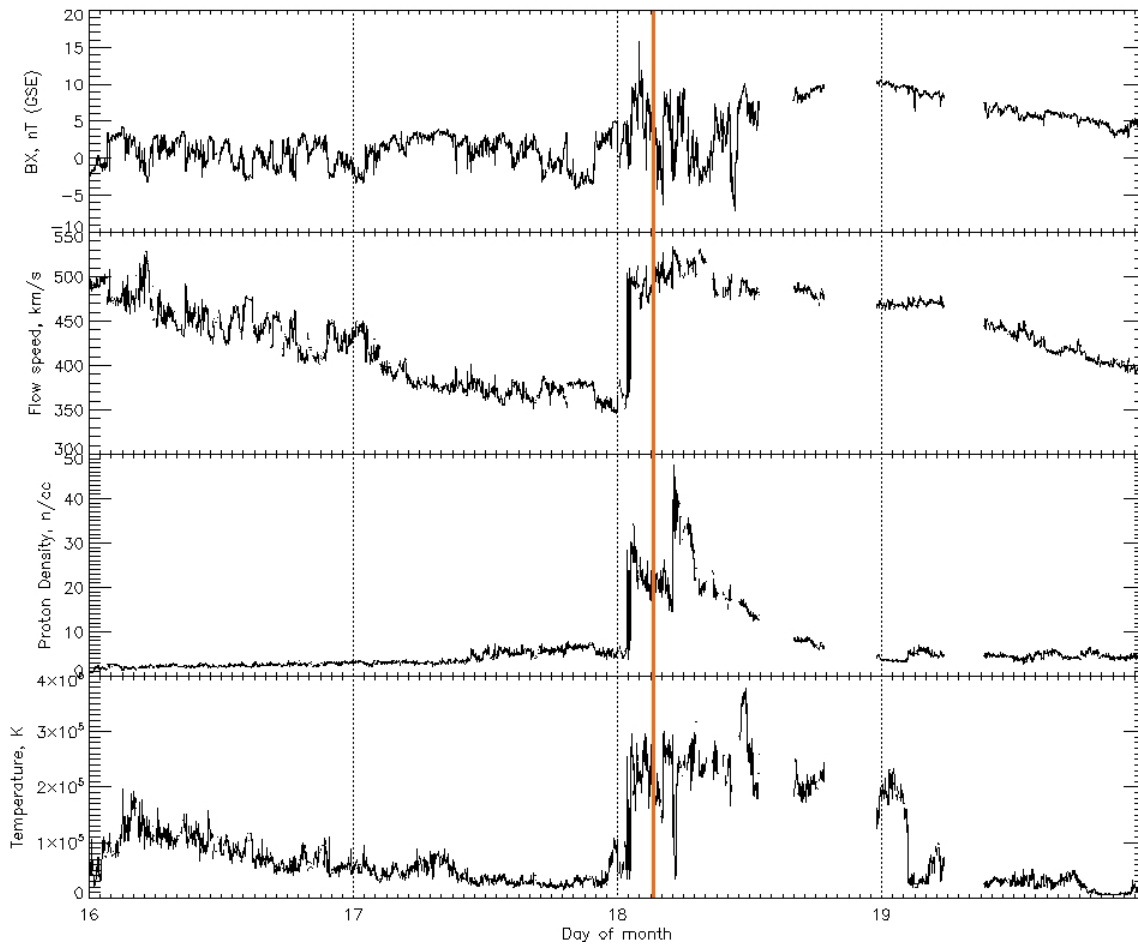
Figure 22. Solar wind flow speed, proton density, temperature and on top the *Bx*-component of the IMF for the period April 16 to April 19, 2001. The orange line marks the onset of the solar proton event that was measured on April 18, 2001. A few hours before, the rapid jump in the solar wind parameters, indicating the passage of an interplanetary shock. Source: OMNIWeb.

The heliographic longitude of the solar wind source regions were calculated from the available solar wind flow speed and the latitudinal source region positions were then identified from SOHO/EIT 195 images which reveal coronal holes as dark areas. However, this was not in all cases uniquely possible. From the positions of the magnetically connected regions, the distance to the identified CME source regions of the proton events was calculated for 66 events. The reading errors of ±5° assumed for the longitude and latitude estimate of the CME source regions and the reading error of ±10° assumed for the longitude and latitude of the identified solar wind source regions, yield error estimates up to about ±11°.

From the calculated distances to the magnetic connection, the two-dimensional and three-dimensional magnetic connection can be analyzed. In Figure 23 the proton peak flux is plotted as a function of the longitudinal distance (upper diagram) and absolute surface distance (lower diagram) of the CME source region to the magnetic connection region of the solar wind at event onset.

The data are divided into three CME speed intervals: $v < 1000$ km/s, $1000 < v < 2000$ km/s and $v > 2000$ km/s. Most of the events scatter about a value of 0°, i.e. the solar wind source region was close to the CME source region. Events to the west fall off in intensity more rapidly than eastern events. This can be interpreted as longer times for particle acceleration being provided through eastern events with respect to the solar wind source region, especially in cases of very fast CMEs and shocks. The highest proton fluxes did occur for longitudes of -80° to 0°, with 40° to 80° corresponding to near disk centered CME source regions with respect to the Sun-Earth line. The bottom diagram shows that an absolute magnetic distance does not provide more information on the proton intensity behaviour. This likely needs further investigation to separate latitudinal and longitudinal effects, as addressed, e.g., by Rouillard et al. 2012.

The CME binning in Figure 23 was very rough and also the longitudinal range has been broadened to include also far easter events for fitting the proton fluxes for different classes of CME speeds in dependence of the longitudinal distance to the CME source region east and west of the CME onset site. The results are shown in Figure 24 in the top diagram. If the fit is applied to space weather radiation hazard warnings, it is suggested to apply worst case flux increase factors to the fit, as shown in Figure 25 for a factor of 10. The diagrams reveal that eastern located fast CMEs have slower flux decreases to the east than to the west of the solar wind connection site. The diagram substantiates the importance of identifying the source region of solar activity, i.e. of fast CMEs and their associated shock waves, to forecast the intensities of solar energetic particle events, by focussing on proton events.

The derived fitting formula is: $$f(x)=A_0 \exp(-z^2/2)$$

With: $z=(x-A_1)/A_2$

A_0 [pfu], A_1 [°], A_2 [°], x [°] (i.e. CME onset site longitude - solar source region longitude)

1: v<1000 km/s $A_{0,1,2}$=[1.58;-20.19;62.24]

2: v=1000-1500 km/s $A_{0,1,2}$=[2.18;-18.91;91,7]

3: v=1500-1700 km/s $A_{0,1,2}$=[3.07;-18.88;48.9]

4: v=1700-2200 km/s $A_{0,1,2}$=[3.45;-43.08;77.02]

5: v>2200 km/s $A_{0,1,2}$=[3.59;-53.8;111.62]
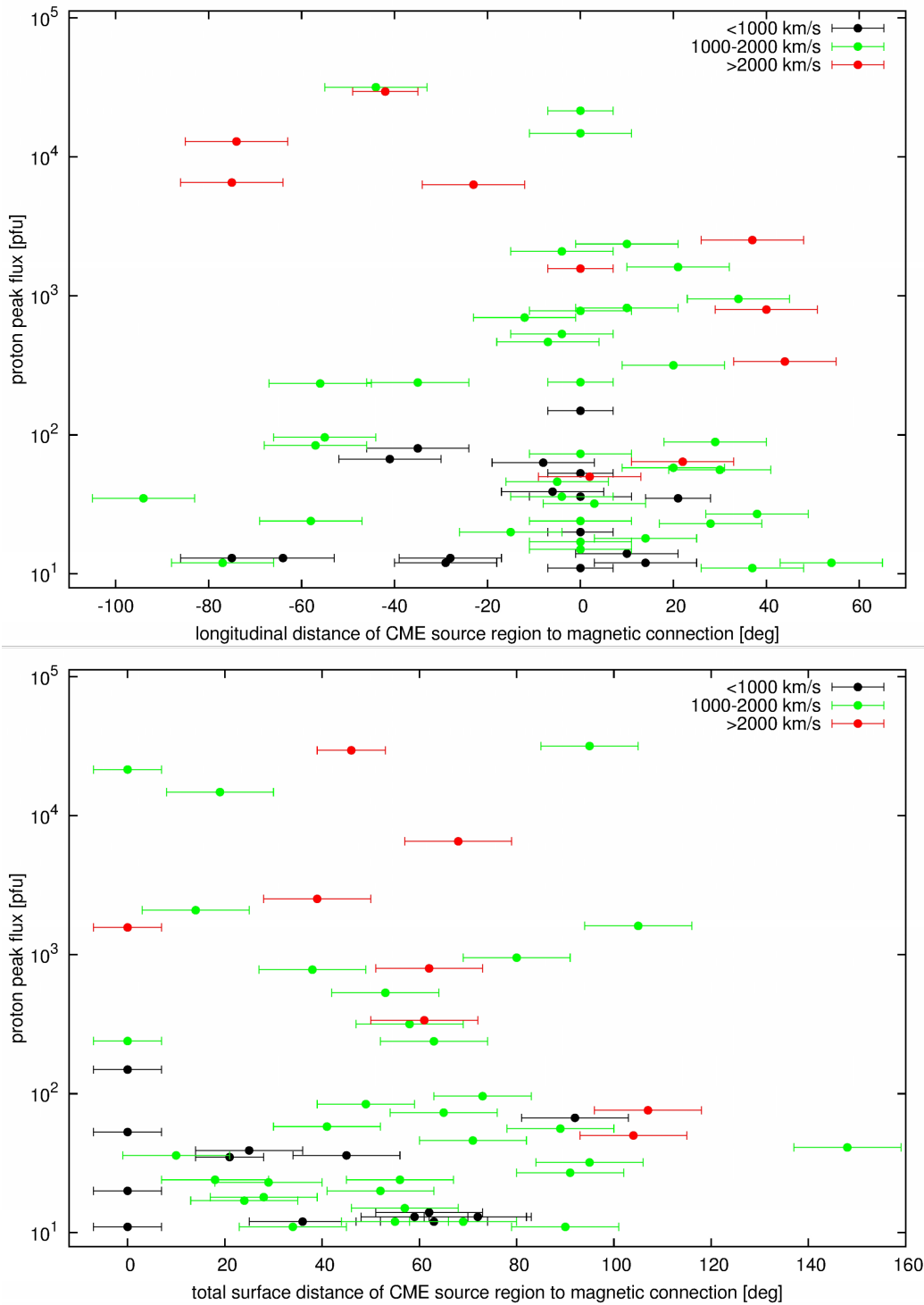
Figure 23. Proton peak flux as a function of longitudinal distance (top) and absolute surface distance (bottom) of the CME source region to the solar wind source regions at times of proton event onset. The data are divided into three CME speed intervals, differently coloured.
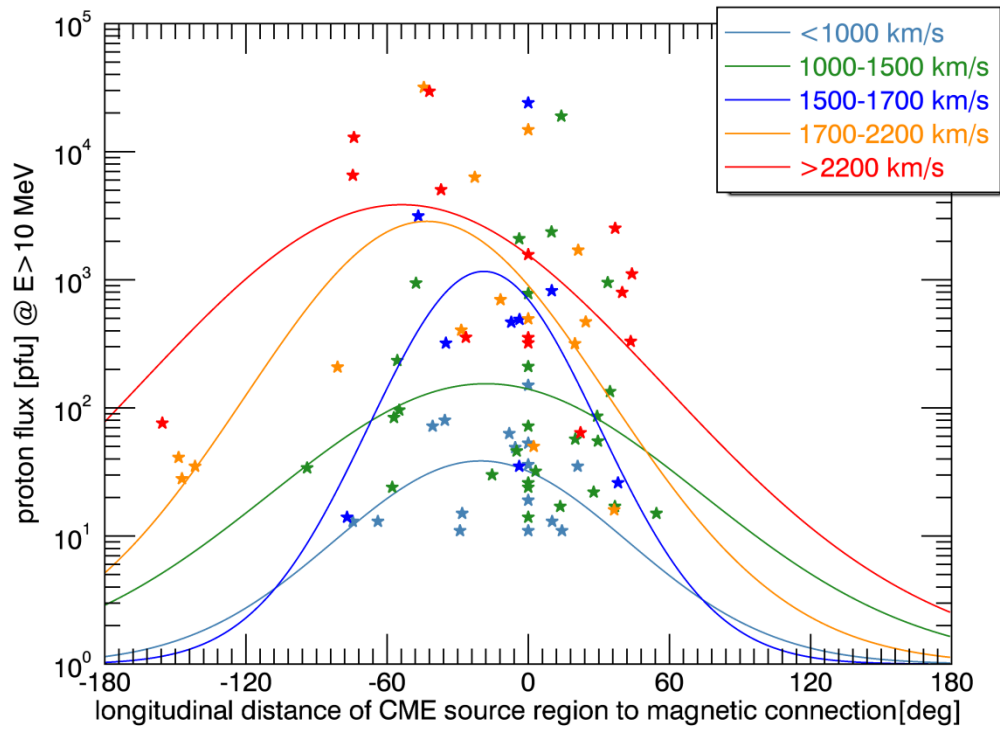
Figure 24. Proton peak flux as a function of longitudinal distance of the CME source region to the solar wind source regions, i.e. in dependence on the magnetic connection. The data are divided into five CME speed intervals which are coloured differently.
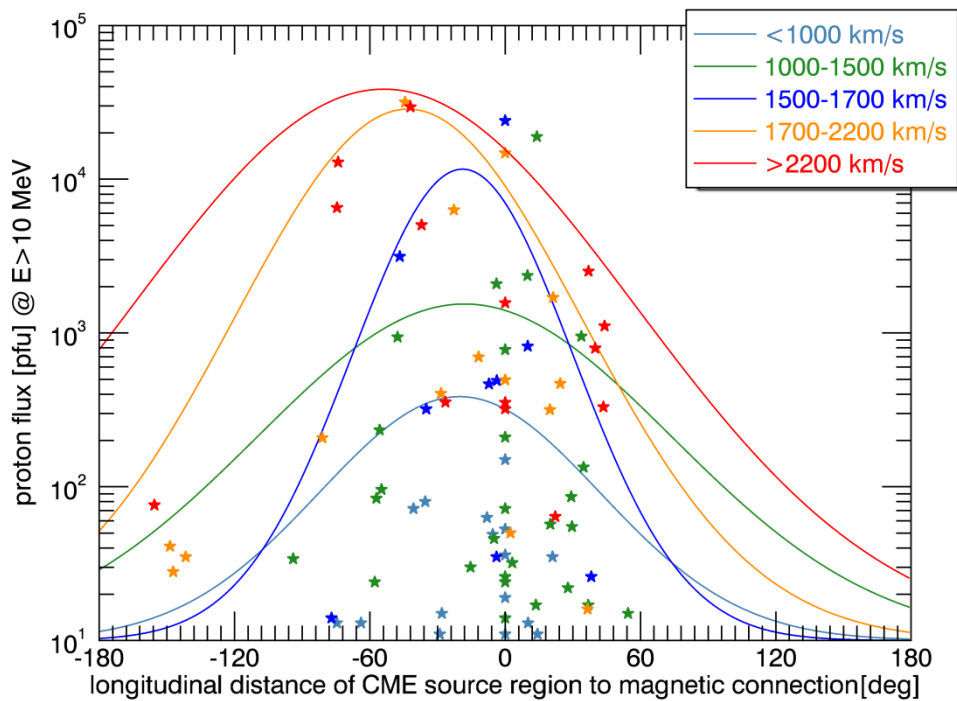
Figure 25. Same fits as in Figure 24 but with a worst case factor of 10 included.

6. Comparison of results with multipoint space observations

In a case study Prise et al. (2014) have investigated within the eHeroes consortium the dependence of solar energetic particles on the longitudinal separation based on multipoint measurements from the STEREO A and B satellites for a fast CME on 3 November 2011. Both STEREO spacecraft were separated more than 90° from the Sun-Earth line and observed the CME from different perspectives, i.e. on-disk with STEREO-B and at the limb with STEREO-A as shown in Figure 26.
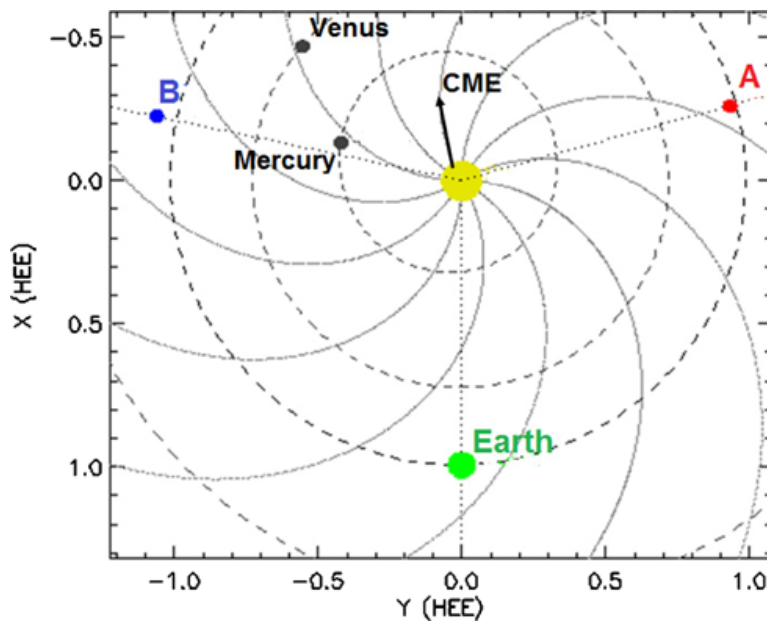
Figure 26. Positions of STEREO-A, STEREO-B, and Earth on 3 November 2011. The direction of the erupting CME is indicated by the black arrow and the Parker spiral is also overlaid. This is a modified version of the plot found at http://stereo-ssc.nascom.nasa. gov/cgi-bin/make_where_gif.

The CME speed was determined to 972 km/s as limb CME in the STEREO/SECCHI COR 2 field of view. In agreement with the fitting plots shown in Figure 24, and neglecting different detector techniques and the orbit of GOES, one would expect STEREO-A to measure a proton flux of the order of 2 or below which is in rough agreement with Figure 27 showing the proton fluxes measured by the IMPACT instrument on STEREO-A and B in a comparable range between 13-100 MeV. The expected flux for STEREO-B, roughly 60° west of the CME is in the range 10-100, which is in rough agreement with the measurements from STEREO-B and well covered by the worst case fit scenario.
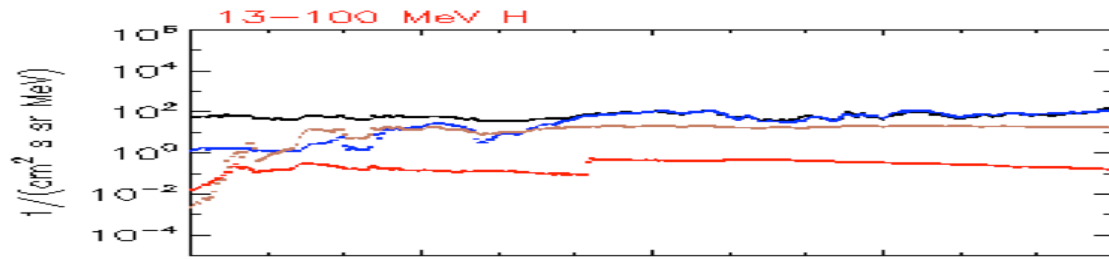
Figure 27. Measurements of proton fluxes at STEREO-A and B for the fast CME on November 3, 2011. In a recent study by Rouillard et al. (2012) the longitudinal properties of an SEP event has been studied in depth too, using multipoint STEREO and near Earth satellite measurements. The event spatial characteristics are shown in Figure 28 (left). The speed of the CME was determined to be in the range 1000-1400 km/s. The longitudinal separation of STEREO A to the CME was about 45° east, about 110° west for STEREO-B and about 160° east for SOHO. The corresponding proton fluxes according to Figure 24 would be 2-3 for SOHO, below 100 for STEREO-A and 20-30 for STEREO-B. This is roughly in agreement with the measurements of STEREO-A and SOHO shown in Figure 28 (right) if one takes the integration of energies into account.
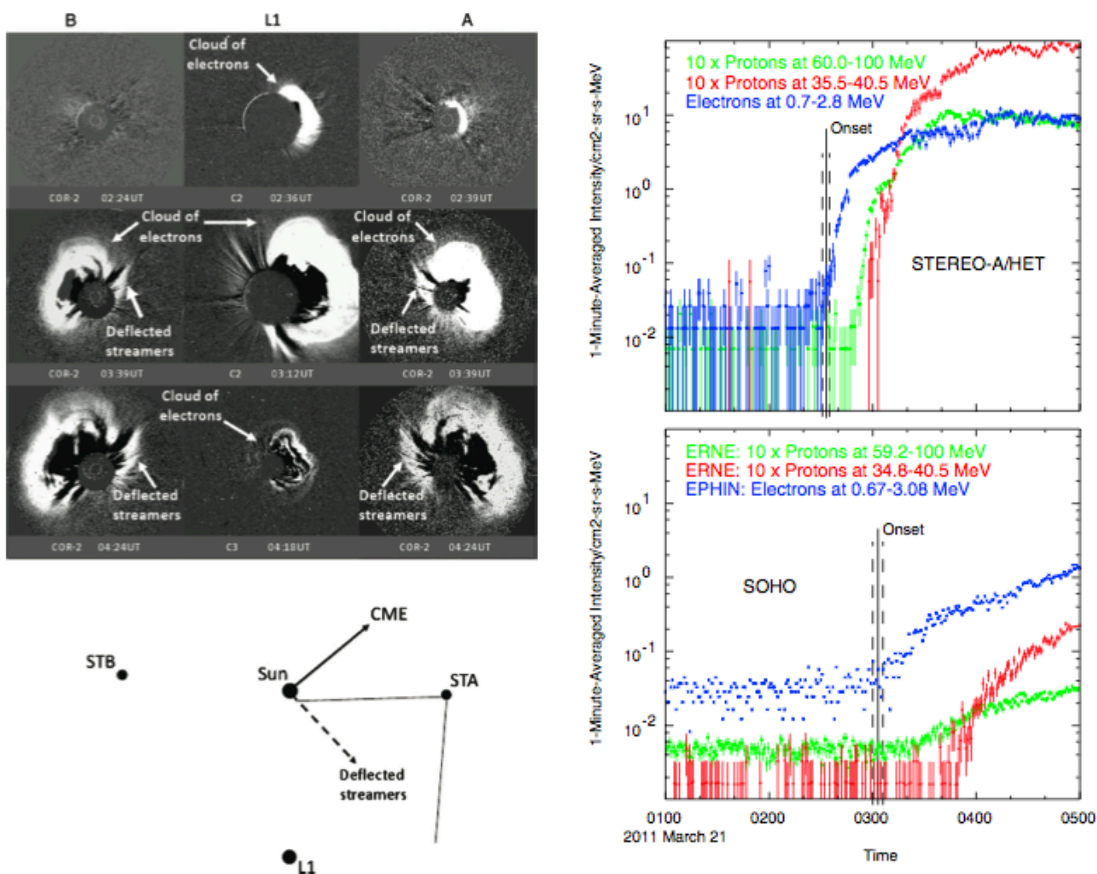
Figure 28. Spatial configuration for the fast CME on March 21, 2011 (left) and proton measurements from STEREO-A and SOHO from Rouillard et al. 2013

7. Extrapolation for space exploration: Mars

From Figures 29 and 30 it can be deduced that the peak flux of a solar proton event is the most significant value for the amount of total high-energy protons measured per event.

Let us now assume an astronaut with a body mass of 70 kg and an exposed body surface of 1 m^2 is on extravehicular activity and the spacesuit provides protection for protons with energies below 10 MeV. During the severe solar radiation storm on July 14, 2000 a total number of about $4 \cdot 10^6$ protons with energies >10 MeV was measured. With $1 \text{ eV} \approx 1.6 \cdot 10^{-19}$ J, the energy of one 10 MeV proton is equal to about $1.6 \ 10^{-12}$ J. Let us further assume that the measured proton flux is similar for the environment of the astronaut. Since pfu is per cm^2, per m^2 a total of $4 \ 10^{10}$ protons would have been measured, which would be $6.4 \ 10^{-2}$ J for the exposed surface of the astronaut. For the body mass of 70 kg, the absorbed energy per mass is $\approx 9.1 \cdot 10^{-4}$ Gy, resulting in an equivalent dose of ≈ 1.83 mSv (the weighting factor for protons is 2) during the period of 5.3 days. At first view, this equivalent dose seems to be low compared to the limit for work-related exposure with 20 mSv, but several missing factors have to be considered. First of all, the total measured protons have energies of >10 MeV, but here exactly 10 MeV per proton was assumed, neglecting protons with higher energies. The shocks of very fast CMEs can accelerate protons to very high energies, up to 300 MeV as showed by Ng & Reames (2008). So concerning the proton energy, 1.83 mSv is the lower limit for the equivalent dose. Furthermore only protons were considered here, but SEP events also involve electrons and heavy ions (e.g. chapter 11 by Facius and Reitz in Bothmer & Daglis 2007). The weighting factor for electrons is 1, but alpha particles and heavy ions have a weighting factor of 20 (Valentin, 2003). So the abundances and energies of heavy ions can drastically increase the equivalent dose. Secondary radiation which is produced when high energetic particles hit metal components, e.g. the hull of the spacecraft, is another factor that increases the effective equivalent dose.

Extrapolation of the estimated radiation doses for a manned mission to Mars can provide important clues for further space exploration. As described in chapter 4, the decrease in proton flux is somewhere below 1/r^{-3} due to the multipole components of the IMF. Assuming that this is the most influencing factor, the proton peak fluxes and the total measured protons per event would decrease accordingly, solar radiation storms at Mars orbit would be a factor of ≥ 0.3 weaker compared to 1 AU. But since interplanetary shocks still accelerate particles after passing 1 AU, there is a not yet measured uncertainty for the estimations based on the analyzed GOES/EPS data. Since the GOES satellites measure the proton flux inside the Earth's magnetosphere and Mars has no significant magnetic field to provide shielding from energetic particles, these factors may have an additional influence.

The influence of the magnetosphere on the GOES/EPS measurements would have to be modelled for a more accurate extrapolation. Also an accurate modelling for the Parker spiral from 1 AU to 1.5 AU would improve the estimation. Proton flux measurements during solar proton events near Mars or at a similar orbital distance could be used for comparison of the proton flux levels. There are several studies on the impact of SEP events at Mars, e.g. from Luhmann et al. (2007), Delory et al. (2012) or Frahm et al. (2013) which analyze the data of Mars orbiting spacecraft like Mars Global Surveyor, for several SEP events. But the relatively small number of events that were measured at Earth and at Mars, as well as the different energy ranges of the measurements, makes it hard to compare their results with the solar proton event parameters obtained here. Multi-point observations using coronagraph data could help to determine the shock parameters (Möstl et al., 2012), especially the shock velocity to eliminate uncertainties due to the use of proxy data. For more comprehensive radiation dose estimation other types of radiation, especially abundances and energy levels of heavy ions have to be included in the analysis. And for a reliable extrapolation of radiation doses for space interesting challenge of future studies.
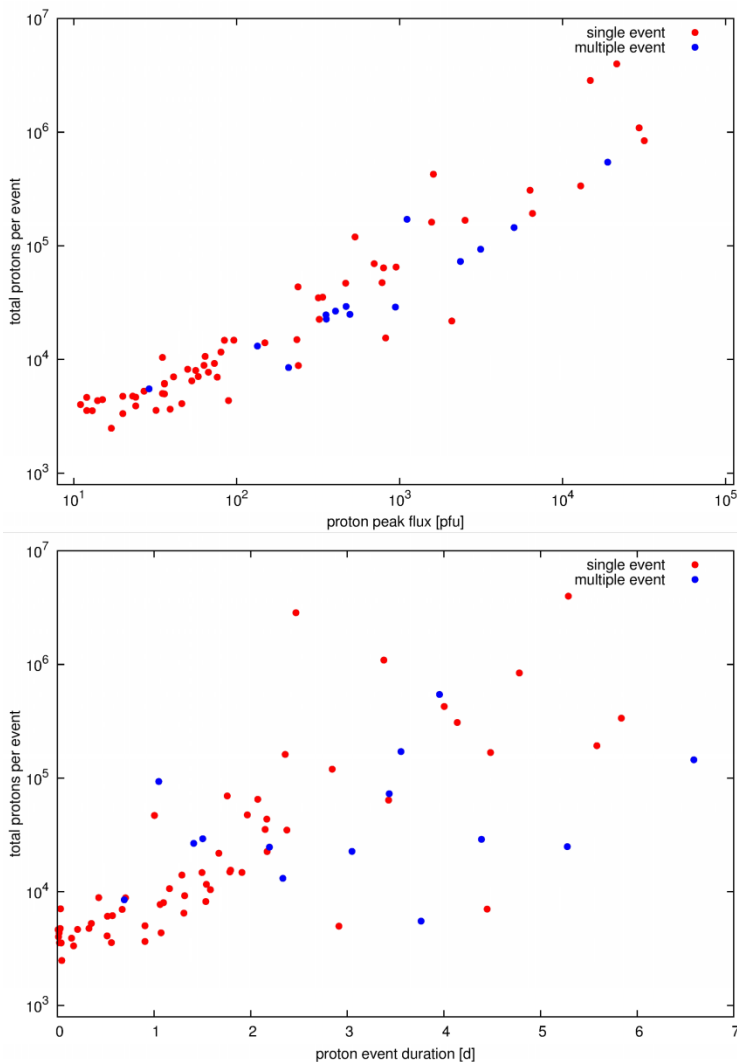
Figure 29. Total protons measured per event as a function of proton peak flux (top) and event duration (bottom). The amount of total protons rises steadily with increasing peak flux.
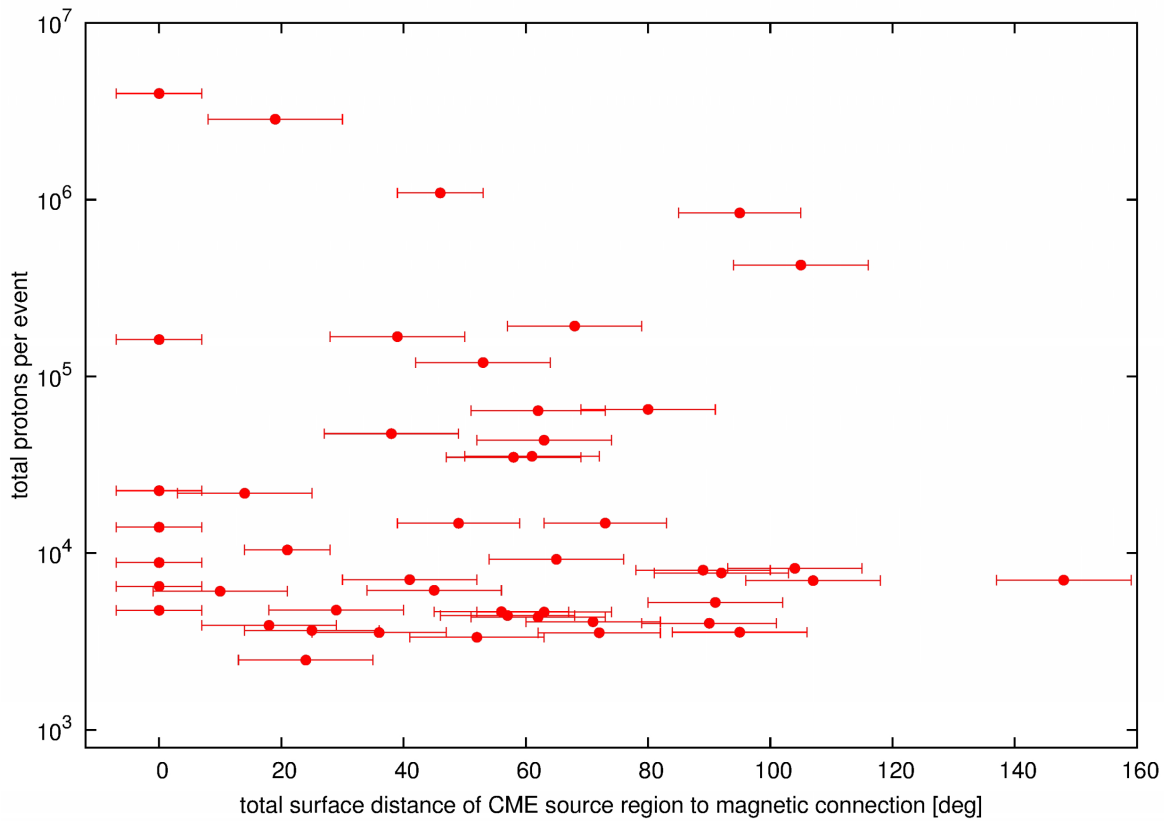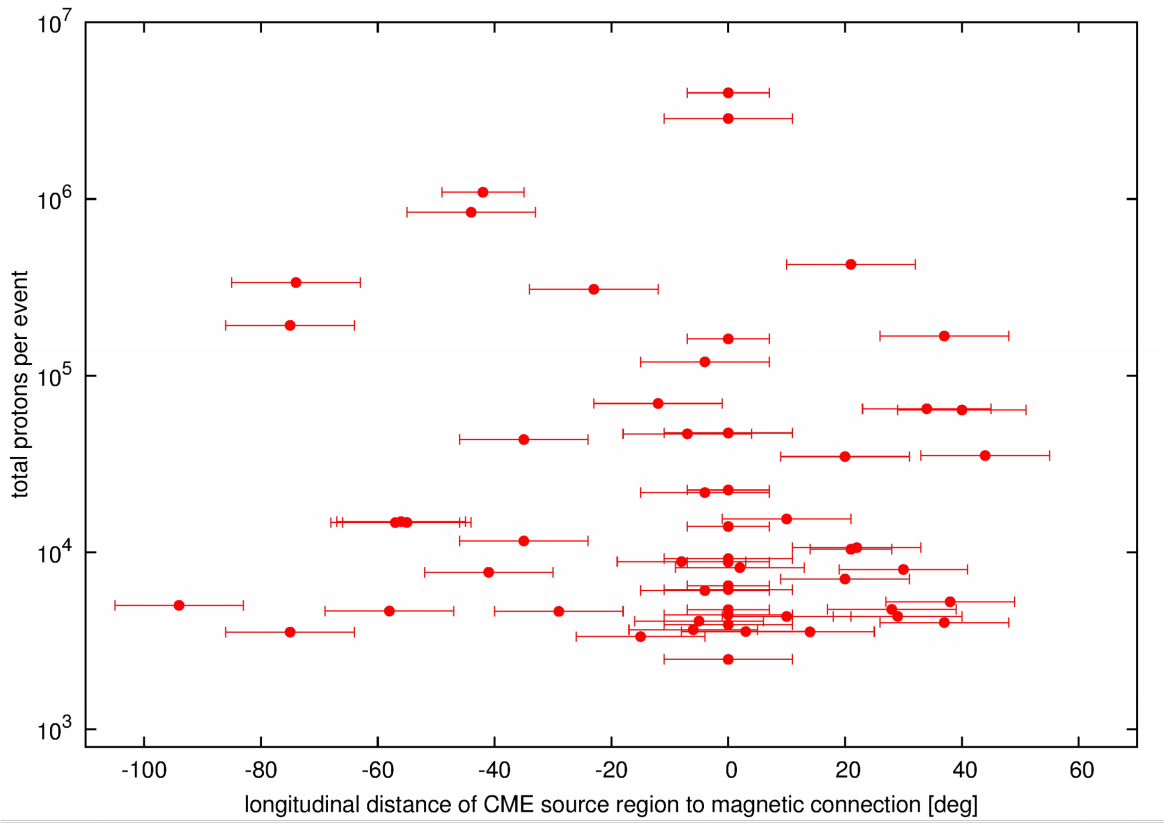
Figure 30. Total measured protons per event as a function of longitudinal distance (top) and total surface distance (bottom) of the CME source region to the solar wind source regions, i.e. magnetic connection.

8 Summary and conclusions

Radiation hazards by intense solar proton events pose a serious threat to satellite systems, aircraft crews and astronauts. In the framework of the eHEROES FP7 project, the goal of task 3.6 in WP3 was to help better understanding the dependence of intense SEP fluxes on the magnetic connection to the solar drivers of the energetic particle events and their onset sites. As baseline for this study the NOAA solar proton event list „Solar Proton Events Affecting the Earth Environment" (http://www.swpc.noaa.gov/ftpdir/indices/SPE.txt), classified by the NOAA space weather scales (http://www.swpc.noaa.gov/NOAAscales/) into the range from minor to extreme radiation storms (S1-S5), was investigated for the time period after launch of ACE in order to be able to analyse the solar wind plasma and IMF conditions measured near Earth orbit at event onset. The solar wind data are required to determine the magnetic connection to the Sun, i.e. the solar wind source regions. The whole NOAA proton event list comprised 252 events from April 1976 to June 2013, for which integrated 5 minutes averages of the various GOES proton flux measurements at energies > 10 MeV had reached three consecutive values of 10 pfu or above. Events which occurred temporarily connected have been treated in this study as one single event. The time period with information on major SEP events provided by the list, together with the solar wind data, span the period November 1997 to March 2012, with 105 SEP entries. These events were then compared with information on CMEs and flares listed in the SOHO LASCO CME catalogue. Taking into account times with missing SOHO data and events without determined CME speeds, the established eHeroes SEP event list includes 81 proton events and a total of 100 associated CMEs. For these events the proton flux data for energies >10 MeV measured by the GOES-08, 11 and 13 satellites were used to determine the characteristic proton event parameters, such as peak flux, event duration and the number of total measured protons per event and the parameters of solar activity were taken compiled from the SOHO LASCO CME catalogue. The source regions of the CMEs were identified using images and movies of the SOHO/LASCO/EIT and MDI, SDO/AIA and HMI, and STEREO/SECCHI instruments. Solar wind data from the ACE and in a few cases as substitutes, from the WIND spacecraft were used to determine the two-dimensional (in longitude) and three-dimensional magnetic connection (the real solar wind source region) to the Sun at the onset of the solar proton events. For the analysis and visualization of the provided proton flux and solar wind data, several IDL routines were created. Fourteen of the proton events of this study had more than one CME associated with them and are called "multiple events", while the other 67 proton are called "single events".

The eHeroes SEP event list was extended with additional information on the position of the associated solar flares and CME source regions, solar wind conditions and the derived magnetic connection. The complete event list is provided as screenshot extract in Appendix A1 of this report. The full version is available in xls-format at http://www.affects-fp7.eu/eHeroes-SEPs/.

The main results of the analysis of the eHeroes SEP list can be summarised as follows:

- Except for one event, all 81 major proton events were associated with fast CMEs with speeds of 750 km/s and above.

- Several CMEs had no associated flare so that it is plausible that these major SEP events were all primarily shock driven events by fast CMEs.

- About 55% of the proton events during the period from November 1997 to March 2012 caused minor radiation storms. The most intense solar proton events generally occur during solar activity maximum, but between solar minimum and maximum intense events were also measured.

- The CME source regions identified were mainly located in the western hemisphere, being almost equally distributed in both hemispheres. The favour of western events is associated with the nominal Parker spiral structure of the solar wind giving rise to close proximities to the onset sites of CMEs in the low corona.

- The fastest CMEs were associated on average with the strongest peak proton fluxes, but the magnetic connection to the CME onset sites have to be taken into account, being of importance for the overall injection time of accelerated particles.

- The most intense proton events were caused by CMEs to the East of the solar wind source regions, i.e. at Earth the CMEs were disk centered.

- The dependence of the proton fluxes, f, on the magnetic connection separation, x, between the solar wind source site and CME source region onset site can be expressed as follows:

$$f(x)=A_0 \exp(-z^2/2)$$

With: $z=(x-A_1)/A_2$
A_0 [pfu], A_1 [°], A_2 [°], x [°] (i.e. CME onset site longitude - solar source region longitude)

1: v<1000 km/s	$A_{0,1,2}$=[1.58;-20.19;62.24]	
2: v=1000-1500 km/s	$A_{0,1,2}$=[2.18;-18.91;91,7]	
3: v=1500-1700 km/s	$A_{0,1,2}$=[3.07;-18.88;48.9]	
4: v=1700-2200 km/s	$A_{0,1,2}$=[3.45;-43.08;77.02]	
5: v>2200 km/s	$A_{0,1,2}$=[3.59;-53.8;111.62]	

- For worst case scenarios the formula can be multiplied by a factor of 10 (see also Figures 24, 25).

- For applying the results to other planets, such as Mars, two aspects need to be taken into account: the general flux decrease with r^{-3} and a further acceleration of protons during the outward travel of fast CMEs and their shock waves ahead.

- The worst case proton fluxes of this study and the fitting results can be applied to space weather forecasts.

- Further multipoint space measurements of SEP events are needed, including measurements at Mars, to validate the results of this study.

9   Appendix

The event list is provided as screenshots below. The full version in xls-format is available at http://www.affects-fp7.eu/eHeroes-SEPs/.

NOAA/SWPC Proton Event list

Solar Energetic Particle Events

Year	Month	Start	Maximum	Event duration [d] from GOES data	Proton Flux peak flux (NOAA list)	Proton Flux peak flux (GOES)	overall flux	Region	Day/Time	Central position angle [°]	Angular Width [°]	Linear Speed [km/s]	CME source region hemispheric position
1997	Nov	04/0830	04/1120	1,0625	72	67	7734	W	04/0610	Halo (BA)	360	785	SW
1997	Nov	06/1305	07/0255	2,84375	490	532	119769	W	06/1210	Halo (OA)	360	1556	SW, near limb
1998	Apr	20/1400	21/1205	4,003472	1700	1610	426813	W	20/1007	284	>243	1863	SW, near limb
1998	May	02/1420	02/1650	1,288194	150	149	14025	Halo	02/1406	Halo (BA)	360	938	S, near center
1998	May	06/0845	06/0945	0,704861	210	239	8834	W	06/0829	309	190	1099	SW, near limb
1998	Nov	08/0245	08/0300	0,013889	11	11	52	W limb	07/2054	321	96	750	NW
1999	Apr	24/1804	25/0055	0,559028	32	32	3572	Halo	24/1331	Halo (OA)	360	1495	SW limb *no flare
1999	May	05/1820	05/1955	0,010417	14	12	44	Halo	03/0606	Halo (OA)	360	1584	NE
1999	Jun	04/0925	04/1055	1,159722	64	64	10644	NW	04/0726	289	150	2230	NW limb
2000	Feb	18/1130	18/1215	0,052083	13	13	189	W	18/0954	286	118	890	center
2000	Apr	04/2055	05/0930	1,097222	55	56	8011	W	04/1632	Halo (OA)	360	1188	NW, near limb
2000	Jun	07/1335	08/0940	1,496528	84	84	14759	Halo	06/1554	Halo (BA)	360	1119	NE, near center
2000	Jun	10/1805	10/2045	0,513889	46	46	4094	Halo	10/1708	Halo (OA)	360	1108	NW
2000	Jul	14/1045	15/1230	5,288194	24000	21500	3985187	NW	14/1054	Halo (S)	360	1674	center
2000	Jul	22/1320	22/1405	0,197917	17	18	353	NW	22/1154	259	>229	1230	NW
2000	Aug	11/1650	11/1740	0,006944	17	11	30	NW limb	11/0738	273	70	1071	NW limb
2000	Sep	12/1555	13/0340	2,166667	320	238	43546	Halo	12/1154	Halo (BA)	360	1550	S center
2000	Oct	16/1125	16/1840	0,013889	15	12	56	Halo	16/0727	Halo (OA)	360	1336	W limb
2000	Oct	26/0040	26/0340	0,079861	15	13	278	Halo	25/0826	Halo (OA)	360	770	N-NW
2000	Nov	08/2350	09/1555	2,46875	14800	14800	2850290	Halo	08/2306	271	>170	1738	NW limb
2000	Nov	24/1520	26/2030	4,388889	940	942	28888	Halo	24/0530	Halo	360	1289	N center

SOHO LASCO CME Catalog data — associated CMEs

Year	Month	Start	End	Duration	Val1	Val2	Number	Dir	Date	Halo	Deg	Value	Location
								Halo	24/1530	Halo (BA)	360	1245	N center
								Halo	24/2206	Halo (OA)	360	1005	N center
								Halo	25/0131	Halo (OA)	360	2519	NE
								W	26/0630	286	227	984	NW
								Halo	26/1706	Halo (OA)	360	980	NW
2001	Jan	28/2025	29/0655	0,90625	49	39	3655	Halo	28/1554	Halo	360	916	W, near limb
2001	Mar	29/1635	30/0610	1,583333	35	35	10428	Halo	29/1026	Halo (BA)	360	942	N center
2001	Apr	02/2340	03/0745	3,555556	1110	1110	171019	NW	02/2206	261	244	2505	NW limb
									03/0326	108	292	1613	E limb
2001	Apr	10/0850	11/2055	3,048611	355	355	22677	Halo	10/0530	Halo (OA)	360	2411	S center
									11/1331	Halo (BA)	360	1103	SW
									12/1031	Halo (OA)	360	1184	SW
2001	Apr	15/1410	15/1920	2,072917	951	951	65090	W	15/1406	245	167	1199	SW limb
2001	Apr	18/0315	18/1045	2,170139	321	321	22592	SW	18/0230	Halo (OA)	360	2465	far SW limb
2001	Apr	28/0430	28/0500	0,03125	57	58	7075	Halo	26/1230	Halo (OA)	244	1006	N-NW
2001	May	07/1915	08/0755	0,166667	30	20	3339	NW	07/1206	286	205	1223	W limb
2001	Sep	15/1435	15/1455	0,020833	11	12	3552	SW	15/1154	129	67	464	SW, near limb
2001	Sep	24/1215	25/2235	5,836806	12900	12900	336650	Halo	24/1030	Halo (OA)	360	2402	SE, near center
2001	Oct	01/1145	02/0810	3,434028	2360	2360	72883	SW	01/0530	Halo (OA)	360	1405	SW limb
2001	Oct	19/2225	19/2235	0,006944	11	12	4637	Halo	19/1650	Halo (BA)	360	901	NW
2001	Oct	22/1910	22/2130	0,208333	24	24	4662	SE	22/1506	Halo (OA)	360	1336	SE, near center
2001	Nov	04/1705	06/0215	4,78125	31700	31700	84122B	Halo	04/1635	Halo (BA)	360	1810	W
2001	Nov	19/1230	20/0010	0,90625	34	35	5018	Halo	17/0530	Halo (OA)	360	1379	SE
2001	Nov	22/2320	24/0555	3,954861	18900	18900	543741	Halo	22/2030	Halo (OA)	360	1443	SW
								Halo	22/2330	Halo (BA)	360	1437	SW
2001	Dec	26/0605	26/1115	1,965278	779	780	47420	W	26/0530	281	>212	1446	W, near limb
2001	Dec	29/0510	29/0815	0,670139	76	76	6991	E	28/2030	Halo (OA)	360	2216	SE limb
2002	Feb	20/0730	20/0755	0,017361	13	14	4343	W	20/0630	Halo (OA)	360	952	W limb
2002	Mar	17/0820	17/0850	0,038194	13	13	3550	Halo	15/2306	Halo (BA)	360	957	center
2002	Mar	18/1300	19/0650	1,309028	53	53	6488	Halo	18/0254	Halo (OA)	360	989	W, near center
2002	Mar	20/1510	20/1525	0,027778	19	20	4752	W	19/1154	287	>194	885	W
2002	Mar	22/2020	23/1320	0,010417	16	11	4013	Halo	22/1106	Halo (OA)	360	1750	SW limb
2002	Apr	17/1530	17/1540	0,145833	24	24	3908	Halo	17/0826	Halo (OA)	360	1240	SW
2002	Apr	21/0225	21/2320	4,482639	2520	2520	167894	W	21/0127	Halo (OA)	360	2393	SW limb
2002	May	22/1755	23/1055	1,791667	820	820	15463	Halo	22/0350	Halo (BA)	360	1557	SW, near limb
2002	Jul	07/1830	07/1955	0,326389	22	23	4763	W	07/1130	277	>228	1423	far W limb
2002	Jul	16/1750	17/1600	1,784722	234	234	14935	Halo	15/2030	Halo (BA)	360	1151	center
2002	Jul	22/0655	23/1025	3,763889	28	29	5521	Halo	20/2206	Halo (OA)	360	1941	E limb
								Halo	23/0042	Halo (OA)	360	2285	E limb

Year	Month												
2002	Feb	20/0730	20/0755	0,017361	13	14	4343	W	20/0630	Halo (OA)	360	952	W limb
2002	Mar	17/0820	17/0850	0,038194	13	13	3550	Halo	15/2306	Halo (BA)	360	957	center
2002	Mar	18/1300	19/0650	1,309028	53	53	6488	Halo	18/0254	Halo (OA)	360	989	W, near center
2002	Mar	20/1510	20/1525	0,027778	19	20	4752	W	19/1154	287	>194	885	W
2002	Mar	22/2020	23/1320	0,010417	16	11	4013	Halo	22/1106	Halo (OA)	360	1750	SW limb
2002	Apr	17/1530	17/1540	0,145833	24	24	3908	Halo	17/0826	Halo (OA)	360	1240	SW
2002	Apr	21/0225	21/2320	4,482639	2520	2520	167894	W	21/0127	Halo (OA)	360	2393	SW limb
2002	May	22/1755	23/1055	1,791667	820	820	15463	Halo	22/0350	Halo (BA)	360	1557	SW, near limb
2002	Jul	07/1830	07/1955	0,326389	22	23	4763	W	07/1130	277	>228	1423	far W limb
2002	Jul	16/1750	17/1600	1,784722	234	234	14935	Halo	15/2030	Halo (BA)	360	1151	center
2002	Jul	22/0655	23/1025	3,763889	28	29	5521	Halo	20/2206	Halo (OA)	360	1941	E limb
2002								Halo	23/0042	Halo (OA)	360	2285	E limb
2002	Aug	14/0900	14/1620	0,045139	26	17	2484	NW	14/0230	297	133	1309	W, near limb
2002	Aug	22/0440	22/0940	0,569444	36	36	6164	SW	22/0206	Halo (OA)	360	998	SW, near limb
2002	Aug	24/0140	24/0835	2,375	317	317	34877	W	24/0127	Halo (OA)	360	1913	SW limb
2002	Sep	07/0440	07/1650	0,690972	208	208	8495	Halo	05/1654	Halo (OA)	360	1748	NE, near center
2002								Halo	06/1331	Halo (BA)	360	909	SW
2002	Nov	09/1920	10/0540	1,409722	404	404	26675	SW	09/1331	Halo (OA)	360	1838	SW
2002								SW	10/0330	203	282	1670	SW
2003	Oct	26/1825	26/2235	1,003472	466	466	46972	Halo	26/1754	270	>171	1537	W
2003	Oct	28/1215	29/0615	3,378472	29500	29500	1090363	Halo	28/1130	Halo (S)	360	2459	S center
2003	Nov	02/1105	03/0815	2,357639	1570	1570	161330	Halo	02/1730	Halo (OA)	360	2598	SW, near limb
2003	Nov	04/2225	05/0600	2,194444	353	353	24662	Halo	04/1954	Halo (OA)	360	2657	SW limb
2003	Dec	02/1505	02/1730	1,072917	86	89	4357	Halo	02/1026	261	>150	1393	SW limb
2004	Apr	11/1135	11/1845	0,517361	35	36	6088	SW	11/0430	203	314	1645	SW
2004	Jul	25/1855	26/2250	1,670139	2086	2090	21810	Halo	25/1454	Halo (BA)	360	1333	W
2004	Nov	01/0655	01/0805	0,427083	63	63	8888	W	01/0606	266	146	925	NW
2004	Nov	07/1910	08/0115	5,277778	495	495	24950	Halo	07/1654	Halo (BA)	360	1759	W, near center
2004								Halo	09/1726	Halo (OA)	360	2000	NW
2004								Halo	10/0222	Halo (OA)	360	3387	

2005	Jan	16/0210	17/1750	6,586906	5040	5040	144818	Halo	15/2306	Halo	360	2861	N center
								Halo	17/0930	Halo	360	2094	NW
								Halo	17/0954	Halo	360	2547	NW
								Halo	19/0829	Halo	360	2020	NW
2005	May	14/0525	15/0240	1,048611	3140	3140	93234	Halo	13/1712	Halo	360	1689	N center
								W	14/2056	261	115	786	SW limb
2005	Jul	14/0245	15/0345	2,333333	134	134	13127	Halo	13/1430	Halo	360	1423	far W limb
								Halo	14/1054	Halo	360	2115	NW limb
2005	Jul	27/2300	29/1715	4,447917	41	41	7037	Halo	27/0454	Halo	360	1787	E limb
2005	Aug	22/2040	23/1045	2,149306	337	330	35311	Halo	22/1730	Halo	360	2378	SW, near limb
2006	Dec	13/0310	13/0925	1,756944	698	698	69660	Halo	13/0254	Halo	360	1774	SW
2010	Aug	14/1230	14/1245	0,017361	15	14	4435	W	14/1012	Halo	360	1205	NW, near limb
2011	Mar	08/0105	08/0800	1,534722	50	50	8197	NW	07/2000	Halo	360	2125	NW, near limb
2011	Jun	07/0820	07/1820	1,315972	73	72	9234	SW	07/0649	Halo	360	1255	SW, near limb
2011	Aug	04/0635	05/2150	1,909722	96	96	14799	NW	04/0412	Halo	360	1315	NW
2011	Aug	09/0845	09/1210	0,350694	27	26	5262	NW	09/0812	Halo	360	1610	NW limb
2011	Sep	23/2255	26/1155	2,913194	36	35	4980	NE	22/1048	Halo	360	1905	E limb
2011	Nov	26/1125	27/0125	1,541667	80	80	11613	NW	26/0712	Halo	360	933	W-NW
2012	Jan	23/0530	24/1530	4,138889	6314	6310	306639	Halo	23/0400	Halo	360	2175	NW
2012	Jan	27/1905	28/0205	3,427083	796	796	63998	Halo	27/1827	Halo	360	2508	NW limb
2012	Mar	07/0510	08/1115	5,583333	6530	6530	192938	Halo	07/0024	Halo	360	2684	NE
2012	Mar	13/1810	13/2045	1,503472	469	469	29280	Halo	13/1736	Halo	360	1884	NW

Bibliography

Bemporad, A. & Mancuso, S. (2010) First Complete Determination of Plasma Physical Parameters Across a Coronal Mass Ejection-driven Shock. ApJ, 720, 130–143.

Bothmer, V. (1999) Solar Corona, Solar Wind Structure and Solar Particle Events. In *Proc. of ESA Workshop on Space Weather Nov. 1998, ESA WPP-155, ISSN 1022-6656, 117-126, 1999.*

Bothmer, V. & Daglis, I. A. (2007) *Space Weather-Physics and Effects*. Springer Praxis Books, Praxis Publishing Ltd, Chichester, Berlin, Heidelberg.

Brueckner, G. E., Howard, R. A., Koomen, M. J., Korendyke, C. M., Michels, D. J., Moses, J. D., Socker, D. G., Dere, K. P. et al. (1995) The Large Angle Spectroscopic Coronagraph (LASCO). Sol. Phys., 162, 357–402.

Cane, H. V. & Lario, D. (2006) An Introduction to CMEs and Energetic Particles. Space Sci. Rev., 123, 45–56.

Cane, H. V., Mewaldt, R. A., Cohen, C. M. S. & von Rosenvinge, T. T. (2006) Role of flares and shocks in determining solar energetic particle abundances. *Journal of Geophysical Research (Space Physics)*, 111, 6.

Cliver, E. W. & Cane, H. V. (2002) The last word. *EOS Transactions*, 83, 61.

Delory, G. T., Luhmann, J. G., Brain, D., Lillis, R. J., Mitchell, D. L., Mewaldt, R. A. & Falkenberg, T. V. (2012) Energetic particles detected by the Electron Reflectometer instrument on the Mars Global Surveyor, 1999-2006. *Space Weather*, 10, 6003.

eHEROES Consortium (2011) *Environment for Human Exploration and RObotic Experimentation in Space - Description of Work*.

Fermi, E. (1949) On the Origin of the Cosmic Radiation. *Physical Review*, 75, 1169–1174.

Frahm, R. A., Sharber, J. R., Winningham, J. D., Elliott, H. A., Howard, T. A., DeForest, C. E., Odstrcˆil, D., Kallio, E. et al. (2013) Solar energetic particle arrival at Mars due to the 27 January 2012 solar storm. In *American Institute of Physics Conference Series*, edited by G. P. Zank, J. Borovsky, R. Bruno, J. Cirtain, S. Cranmer, H. Elliott, J. Giacalone, W. Gonzalez, G. Li, E. Marsch, E. Moebius, N. Pogorelov, J. Spann & O. Verkhoglyadova, vol. 1539 of *American Institute of Physics Conference Series*.

Fränz, M. & Harper, D. (2002) Heliospheric coordinate systems. Planet. Space Sci., 50, 217–233.

Gopalswamy, N., Yashiro, S., Michalek, G., Stenborg, G., Vourlidas, A., Freeland, S. & Howard, R. (2009) The SOHO/LASCO CME catalogue. *Earth Moon and Planets*, 104, 295–313.

Hanslmeier, A. (2002) Solar energetic phenomena and radiation hazards to biological systems. In *Exo-Astrobiology*, edited by H. Lacoste, vol. 518 of *ESA Special Publication*.

Howard, R. A., Moses, J. D., Vourlidas, A., Newmark, J. S., Socker, D. G., Plunkett, S. P., Korendyke, C. M., Cook, J. W. et al. (2008) Sun Earth Connection Coronal and Heliospheric Investigation (SECCHI). Space Sci. Rev., 136, 67–115.

Kahler, S. W. & Vourlidas, A. (2013) A Comparison of the Intensities and Energies of Gradual Solar Energetic Particle Events with the Dynamical Properties of Associated Coronal Mass Ejections. ApJ, 769, 143.

Lemen, J. R., Title, A. M., Akin, D. J., Boerner, P. F., Chou, C., Drake, J. F., Duncan, D. W., Edwards, C. G. et al. (2012) The Atmospheric Imaging Assembly (AIA) on the Solar Dynamics Observatory (SDO). Sol. Phys., 275, 17–40.

Luhmann, J. G., Zeitlin, C., Turner, R., Brain, D. A., Delory G., Lyon, J. G. & Boynton, W. (2007) Solar energetic particles in near-Mars space. *Journal of Geophysical Research (Planets)*, 112, 10001.

Moses, D., Clette, F., Delaboudinière, J.-P., Artzner, G. E., Bougnet, M., Brunaud, J., Carabetian, C., Gabriel, A. H. et al. (1997) EIT Observations of the Extreme Ultraviolet Sun. Sol. Phys., 175, 571–599.

Möstl, C., Farrugia, C. J., Kilpua, E. K. J., Jian, L. K., Liu, Y., Eastwood, J. P., Harrison, R. A., Webb, D. F. et al. (2012) Multi-point Shock and Flux Rope Analysis of Multiple Interplanetary Coronal Mass Ejections around 2010 August 1 in the Inner Heliosphere. ApJ, 758, 10.

Neergaard Parker, L. & Zank, G. P. (2012) Particle Acceleration at Quasi- parallel Shock Waves: Theory and Observations at 1 AU. ApJ, 757, 97.

Ng, C. K. & Reames, D. V. (2008) Shock Acceleration of Solar Energetic Protons: The First 10 Minutes. ApJ, 686, L123–L126.

Ogilvie, K. W., Chornay, D. J., Fritzenreiter, R. J., Hunsaker, F., Keller, J., Lobell, J., Miller, G., Scudder, J. D. et al. (1995) SWE, A Comprehensive Plasma Instrument for the Wind Spacecraft. Space Sci. Rev., 71, 55–77.

Parker, E. N. (1958) Dynamics of the Interplanetary Gas and Magnetic Fields. ApJ, 128, 664.

Pesnell, W. D., Thompson, B. J. & Chamberlin, P. C. (2012) The Solar Dynamics Observatory (SDO). Sol. Phys., 275, 3–15.

Plunkett, S. P., Thompson, B. J., Howard, R. A., Michels, D. J., St. Cyr, O. C., Tappin, S. J., Schwenn, R. & Lamy, P. L. (1998) LASCO observations of an Earth-directed coronal mass ejection on May 12, 1997. Geo- phys. Res. Lett., 25, 2477–2480.

Prise, A.J., Harra, L.K., Matthews, S.A., Long, D.M., Aylward, A.D. (2014), An investigation of the CME of 3 November 2011 and associated widespread solar energetic particle event, Solar Phys., 289:1731-1744.

Reames, D. V. (1999) Particle acceleration at the Sun and in the heliosphere. Space Sci. Rev., 90, 413–491.

Reames, D. V. (2001) SEPs: Space Weather Hazard in Interplanetary Space. *Geophysical Monograph*, 125.

Reames, D. V. (2004) Solar energetic particle variations. *Advances in Space Research*, 34, 381–390.

Reames, D. V., Kahler, S. W. & Ng, C. K. (1997) Spatial and Temporal Invariance in the Spectra of Energetic Particles in Gradual Solar Events. ApJ, 491, 414.

Roberts, C. E. (2002) The SOHO Mission L1 Halo Orbit Recovery From the Attitude Control Anomalies of 1998, Libration Point Orbits and Applications Conference Parador d'Aiguablava, Girona, Spain.

A. P. Rouillard1, Sheeley, N. R., Tylka, A., Vourlidas, A., Ng, C.K., Rakowski, C., Cohen, C. M. S., Mewaldt, R.A., Mason, G.M., Reames, D., Savani, N.P., StCyr, O.C., Szabo, A., (2012) The longitudinal properties of a solar energetic particle event investigated using modern solar imaging, ApJ, 752, 44.

Scherrer, P. H., Bogart, R. S., Bush, R. I., Hoeksema, J. T., Kosovichev, A. G., Schou, J., Rosenberg, W., Springer, L. et al. (1995), The Solar Oscillations Investigation - Michelson Doppler Imager. Sol. Phys., 162, 129–188.

Scherrer, P. H., Schou, J., Bush, R. I., Kosovichev, A. G., Bogart, R. S., Hoeksema, J. T., Liu, Y., Duvall, T. L. et al. (2012) The Helioseismic and Magnetic Imager (HMI) Investigation for the Solar Dynamics Observatory (SDO). Sol. Phys., 275, 207–227.

Stassinopoulos, E. G. & Raymond, J. P. (1988) The space radiation environment for electronics. *IEEE Proceedings*, 76, 1423–1442.

Stone, E. C., Frandsen, A. M., Mewaldt, R. A., Christian, E. R., Margolies, D., Ormes, J. F. & Snow, F. (1998) The Advanced Composition Explorer. Space Sci. Rev., 86, 1–22.

Swanson, D. G. (1989) Plasma waves, published by CRC press.

Thompson, W. T. (2006) Coordinate systems for solar image data. A&A, 449, 791–803.

Tripathi, D., Bothmer, V. & Cremades, H. (2004) The basic characteristics of EUV post-eruptive arcades and their role as tracers of coronal mass ejection source regions. A&A, 422, 337–349.

Valentin, J. (2003) *Relative Biological Effectiveness (RBE), Quality Factor (Q), and Radiation Weighting Factor (Wr)*. Annals of the ICRP, Pergamon.

Vourlidas, A., Wu, S. T., Wang, A. H., Subramanian, P. & Howard, R. A. (2003) Direct Detection of a Coronal Mass Ejection-Associated Shock in Large Angle and Spectrometric Coronagraph Experiment White-Light Images. ApJ, 598, 1392–1402.

Zeeman, P. (1897) On the Influence of Magnetism on the Nature of the Light Emitted by a Substance. *ApJ*, 5, 332.